JOURNAL OF GEOPHYSICAL RESEARCH: SOLID EARTH, VOL. 118, 1216–1239, doi:10.1002/jgrb.50107, 2013

Tidal modulation and back-propagating fronts in slow slip events simulated with a velocity-weakening to velocity-strengthening friction law

J. C. Hawthorne[1,2] and A. M. Rubin[1]

Received 20 August 2012; revised 16 January 2013; accepted 26 January 2013; published 26 March 2013.

[1] We examine tidal modulation and back-propagating fronts in simulated slow slip events using a rate and state friction law that is steady state velocity weakening at low slip rates and velocity strengthening at high slip rates. Tidal forcing causes a quasi-sinusoidal modulation of the slip rate during the events, with the maximum moment rate occurring close to or slightly after the maximum applied stress. The amplitude of modulation scales linearly with the tidal load and increases as the tidal period increases relative to the timescale for state evolution. If we choose parameters so that the model matches the observed tidal modulation of slip in Cascadia, it can reproduce only a subset of the stress drops inferred from observations and only in a limited portion of parameter space. The tidal forcing also causes back-propagating fronts to form and move back through the region that has already ruptured. The stress drop that drives these back-propagating fronts sometimes comes from the tidal load and sometimes from a stress recovery that occurs behind the front in tidal and non-tidal simulations. We investigate the slip and propagation rates in the back-propagating fronts and compare them with observations. The modeled fronts propagate too slowly to be good representations of the fronts inferred from tremor observations. For the simulated fronts to propagate at the observed speeds, the stress drops driving them would have to be more than 70% of the stress drop driving the forward-propagating front.

Citation: Hawthorne, J. C., and A. M. Rubin (2013), Tidal modulation and back-propagating fronts in slow slip events simulated with a velocity-weakening to velocity-strengthening friction law, *J. Geophys. Res. Solid Earth*, *118*, 1216–1239, doi:10.1002/jgrb.50107.

1. Introduction

[2] Slow slip events have been observed at a number of plate boundaries over the past 10 years. They have average slip rates of 10 to 100 times the plate convergence rate and last between a few days and a few months. In segments of many subduction zones, events occur episodically at intervals between a few months and several years. In large events in Cascadia and beneath Shikoku and the Kii Peninsula in Japan, the location of tremor and slip propagates along strike during each event, over the course of days to weeks [e.g., *Dragert et al*., 2001; *Obara*, 2002; *Schwartz and Rokosky*, 2007; *Peng and Gomberg*, 2010; *Obara*, 2010; *Bartlow et al*., 2011].

[3] Given the observations, it seems reasonable to model slow slip events by considering frictional sliding on the plate interface. It is still unclear, however, which friction law is most appropriate for modeling these events. Three variants of rate and state friction models are commonly proposed. The first is "standard" velocity-weakening rate and state friction. It allows for episodic slow slip events if the size of the slow slip region is sufficiently tuned [*Liu and Rice*, 2005, 2007; *Rubin*, 2008; *Liu and Rice*, 2009]. The second variant couples standard velocity-weakening friction with shear-induced dilatancy. It allows for slow slip events when the fault zone permeability is relatively low [*Segall and Rice*, 1995; *Suzuki and Yamashita*, 2009; *Liu and Rubin*, 2010; *Segall et al*., 2010; *Yamashita and Suzuki*, 2011]. The final variant, which we will investigate here, uses a friction law that is steady state velocity weakening at low slip speeds but velocity-strengthening speeds higher than a chosen cutoff velocity [*Shibazaki and Iio*, 2003; *Shibazaki and Shimamoto*, 2007; *Beeler*, 2009; *Matsuzawa et al*., 2010; *Shibazaki*, 2010].

[4] A friction law with a velocity-weakening to velocity-strengthening transition has been suggested by some physical models of rate and state friction [e.g., *Brechet and Estrin*, 1994; *Nakatani and Scholz*, 2006; *Beeler*, 2009] and inferred from laboratory experiments on a variety of

[1]Department of Geosciences, Princeton University, Princeton, New Jersey, USA.
[2]Now at Division of Geological and Planetary Sciences, California Institute of Technology, Pasadena, California, USA.

Corresponding author: J. C. Hawthorne, Caltech Seismological Laboratory, 1200 E. California Blvd., MS 252-21, Pasadena, CA 91125, USA. (jessicah@caltech.edu)

2169-9313/13/10.1002/jgrb.50107

geologic and non-geologic materials [e.g., *Dieterich*, 1972; *Shimamoto*, 1986; *Weeks*, 1993; *Reinen et al*., 1994; *Moore et al*., 1997; *Nakatani and Scholz*, 2004]. These experimental and theoretical results are summarized in section 3.9 of *Hawthorne* [2012].

[5] We examined a number of properties of slow slip events simulated with a velocity-weakening to velocity-strengthening friction law in our companion paper [Hawthorne and Rubin, Laterally propagating slow slip events in a rate and state model with a velocity-weakening to-strengthening transition, submitted]. We will refer to that paper as paper 1. In it we identified a part of parameter space that allows the model to reproduce the stress drops, slip velocities, and propagation rates of events in Cascadia and Japan. However, if sufficient tuning is allowed, those observations can also be reproduced by standard velocity-weakening friction and dilatancy models. If we are to determine which, if any, of the proposed models is appropriate for slow slip, we need to compare the model results to additional observations. In this paper, we assess whether a friction law with a velocity-weakening to velocity-strengthening transition can match two such observations. First, we investigate tidal modulation of slow slip. Second, we investigate back-propagating fronts, which can either be strongly associated with or independent of tidal modulation.

[6] Tidal modulation of tremor has been seen at a number of subduction zones. *Shelly et al*. [2007] observed a preferred timing in two events in western Shikoku, and *Ide* [2010] noted a response at the tidal period that varied with location in that region. In eastern Shikoku, bursts of tremor in a number of events occurred preferentially between the maximum Coulomb stressing rate and the maximum Coulomb stress [*Nakata et al*., 2008]. Tremor on the San Andreas Fault was more commonly observed at the maximum tidal shear stress [*Thomas et al.*, 2009, 2012]. In Cascadia, *Rubinstein* [2008] found that variation in the amplitude of tremor seismograms had more energy at the 12.4 h period of the semidiurnal lunar tide than at non-tidal periods. *Lambert et al*. [2009] observed a correlation between tremor occurrence and Coulomb stress beneath Vancouver Island. *Klaus et al.* [2011] found that tremor occurred preferentially at the time of the maximum shear stress in central Cascadia. The timing of increased tremor occurrence varied along strike in a way that was consistent with the along-strike change in the timing of the tidal loading. Using borehole strainmeter data, *Hawthorne and Rubin* [2010] observed that tides modulate slow slip, not just tremor. The slow slip moment rate varied, on average, 20 to 30% above and below the mean moment rate during each 12.4 h tidal period, and the maximum moment rate coincided with the preferred timing of tremor identified by *Wech et al*. [2009]. According to tidal loading calculations, the maximum moment rate preceded the spatially averaged peak shear stress by about 45°, but because the phase of loading varies along strike, the data are also consistent with a peak slip rate that coincides with the maximum shear stressing rate or with the maximum shear stress.

[7] In Cascadia and beneath Shikoku and the Kii Peninsula in Japan, identified tremor locations generally move along strike at 5 to 15 km/d during large events, but during some 1 to 10 h periods, they move back through the region that has already slipped [*Houston et al*., 2011; *Obara et al*., 2012]. In the latter half of this paper, we will assess whether our chosen model can produce aseismic back-propagating fronts that exhibit the propagation rates and spatial extents of these rapid tremor reversals (RTRs). Identified RTRs typically propagate at rates of 20 to 40 times that of the forward-propagating front and travel 30 to 70 km [*Obara*, 2010; *Houston et al*., 2011; *Obara et al*., 2012]. Some sets of RTRs occur periodically at intervals close to the tidal periods [*Obara*, 2010]. Others display no obvious periodicity [*Obara*, 2010; *Houston et al*., 2011; *Obara et al*., 2012].

[8] We design our model to produce slow slip events similar to the large events in Cascadia and beneath Shikoku and the Kii Peninsula, where tidal modulation and back-propagating fronts have been observed. In these regions, the along-strike extent of the slow slip region is several times its along-dip extent [e.g., *Wech et al*., 2009; *Obara*, 2010; *Schmidt and Gao*, 2010]. We simulate events on a line fault, but we adjust the elasticity equations to mimic the elongate geometry characteristic of these regions. As described in paper 1, simulated events propagate in a parameterized "along-strike" direction. They last at least several tidal cycles, since we wish to compare the results with observations of events that last several days to several weeks [e.g., *Dragert et al*., 2001; *Wech et al*., 2009; *Obara*, 2010; *Ide*, 2012].

[9] In section 2, we introduce the chosen friction law and the model geometry. We summarize a few relevant features of the modeled events that are unrelated to tidal modulation and back-propagating fronts in section 3. In section 4, we show that tidal forcing results in a quasi-sinusoidal modulation of the slip rate and estimate the amplitude of modulation as a function of the model parameters. In section 5, we describe the simulated back-propagating fronts and estimate their slip rates and propagation velocities. Finally, in section 6, we compare these behaviors and magnitudes to available observations.

2. Model Definition

2.1. Friction Law

2.1.1. Definition

[10] The frictional strength of our modeled fault is [e.g., *Dieterich*, 2007]

$$\tau(V,\theta) = f^*\sigma + a\sigma \log\left(\frac{V}{V^*}\right) + b\sigma \log\left(\frac{V_c\theta}{D_c} + 1\right). \qquad (1)$$

Here V is the local slip rate. θ is the local state, which is a measure of how well adhered a fault is. σ is the effective normal stress, and a and b are non-dimensional constants. a determines the amplitude of the "direct" velocity effect, and b determines the amplitude of the state evolution effect. D_c is a length scale that controls the slip distance for state evolution. f^* is a reference coefficient of friction, V^* is a reference velocity, and V_c is the cutoff velocity. This law differs from "standard" rate and state friction in that it includes a cutoff on the influence of state on stress, implemented with the "+1" in the final term.

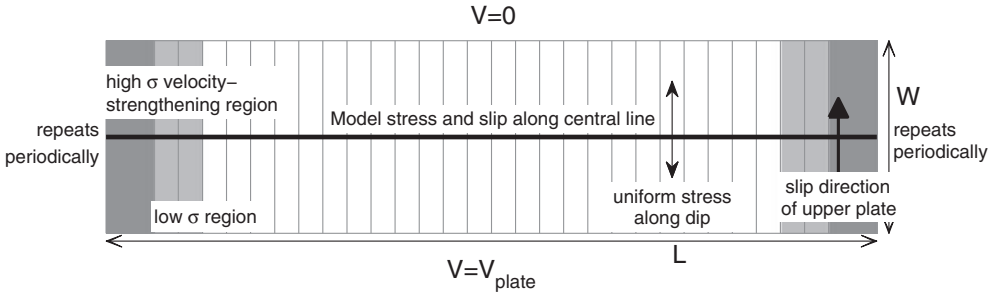

Figure 1. Strip model geometry for elasticity calculations. We assume that stress is uniform along dip and model slip along the central line. The fault slips at the plate rate V_0 downdip of the slow slip region and is locked updip. The model repeats periodically along strike (horizontally).

[11] Depending on the simulation, the evolution of state with time is dictated by either the "aging" law,

$$\frac{\mathrm{d}\theta}{\mathrm{d}t} = 1 - \frac{V\theta}{D_c}, \tag{2}$$

or the "slip" law,

$$\frac{\mathrm{d}\theta}{\mathrm{d}t} = -\frac{V\theta}{D_c}\log\left(\frac{V\theta}{D_c}\right) \tag{3}$$

[e.g., *Ruina*, 1983; *Marone*, 1998]. For both the aging and slip laws, when the fault slips at a constant rate V, state evolves toward a steady state value of D_c/V. The steady state stress as a function of slip velocity is then

$$\tau_{ss}(V) = f^*\sigma + a\sigma\log\left(\frac{V}{V^*}\right) + b\sigma\log\left(\frac{V_c}{V}+1\right). \tag{4}$$

When $V \ll V_c$, the steady state strength decreases with increasing velocity if $a < b$, and the slope of the steady state curve ($d\tau_{ss}/d\log(V)$) tends to $-(b-a)\sigma$. When $V \gg V_c$, the steady state strength increases with increasing velocity, and $d\tau_{ss}/d\log(V)$ tends to $a\sigma$. The boundary between the velocity-weakening and velocity-strengthening portions of the steady state curve lies at the minimum steady state stress, which we call $\tau_{ss\text{-}min}$. From equation (4), it occurs at a velocity of

$$V_{\tau\text{-}min} = V_c\frac{b-a}{a}. \tag{5}$$

2.2. Strip Model Setup

[12] At less than elastodynamic slip speeds, the frictional strength of the fault is equal to the driving stress, which in our model is the sum of the elastic stress due to slip and the assumed tidal loading. To mimic the elongate geometry of the slow slip source region, we approximate the slow slip region as rectangular with along-strike extent L and along-dip extent W, as illustrated in Figure 1. We assume that within this region, stress varies along strike but is uniform along dip. We further assume that the fault slips at a uniform rate V_0 downdip of the slow slip region and that it does not slip updip of the slow slip region. We then solve for the relationship between slip and stress along a one-dimensional grid associated with the fault's central line, as described in paper 1. We couple that relationship with the friction law to run the simulations. For computational efficiency, we perform the elasticity calculations in the wave number domain, and the modeled fault repeats periodically along strike.

[13] The tidal forcing is implemented as an additional stress that is uniform in space and varies sinusoidally in time: $\tau_t = A_t\sin(2\pi t/T_t)$. We equate the sum of the elastic stress due to slip τ_{el} and the sinusoidal forcing τ_t to the frictional strength from equation (1). In each time step, we use the derivative of these equations and the evolution law (equation (2) or (3)) to update the slip rate, state, stress, and slip at each point.

2.3. Parameter Distribution

[14] On most of the fault, a, b, and σ are uniform with a/b between 0.6 and 0.9. In this paper, we will focus on the behavior of large slow slip events in this homogeneous region. However, we do introduce some heterogeneity to allow for the nucleation of events, as described in paper 1 and Appendix A. In all simulations, there is a region with width of $0.5W$ which also obeys equation (1) but has $a > b$ and higher normal stress than the bulk of the fault. In some simulations, the regions adjacent to that purely velocity-strengthening region have lower normal stress than the bulk of the fault.

[15] The chosen cutoff velocity V_c is 100 times the downdip loading rate V_0, so that the simulated events have slip rates a few orders of magnitude larger than V_0. The tidal period T_t is such that there are at least a few periods in each slow slip event. It ranges from $10^{-1}D_c/V_c$ to $10^3D_c/V_c$. The tidal half-amplitude A_t ranges from $0.01b\sigma$ to $0.2b\sigma$. This is between 0.01 and 0.3 times the stress drop in the simulated events. Such values roughly match the observations, as the tidal shear stress in Cascadia is about 1 kPa [e.g., *Lambert et al*., 2009; *Hawthorne and Rubin*, 2010]. This is roughly 0.01 to 0.2 times plausible stress drops in major slow slip events, which are 5 to 100 kPa [e.g., *Szeliga et al*., 2008; *Wech et al*., 2009; *Schmidt and Gao*, 2010].

[16] The chosen along-dip lengths W are large enough that simulations produce periodic slow slip events, according to the constraints described in paper 1. W ranges from 125 to 1000 L_b, where the length scale $L_b = D_c\mu/b\sigma$ and μ is the shear modulus. The upper bound on W/L_b is a computational constraint. The along-strike length L ranges from 3 to $10W$. The model is discretized with a uniform grid spacing. On the bulk of the fault, there are at least eight grid points per L_b in aging law simulations and at least 40 points per L_b in slip law simulations.

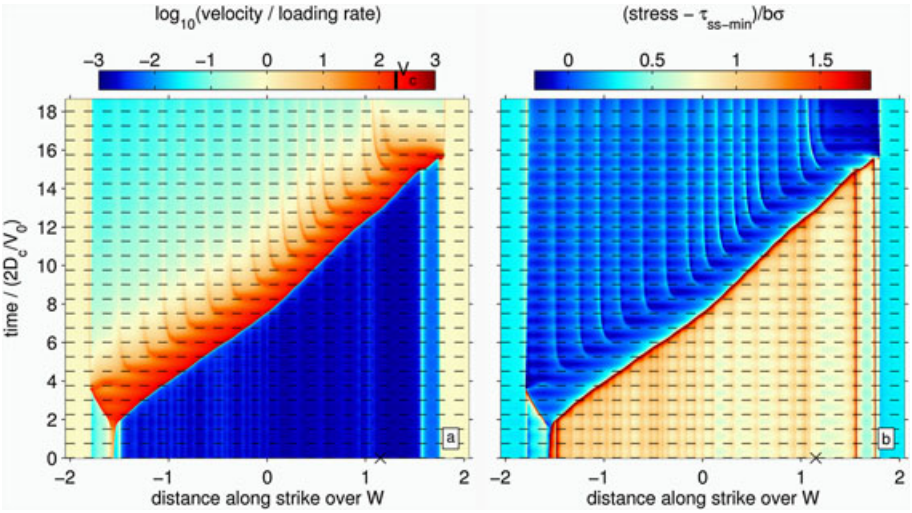

Figure 2. (a) Slip rate and (b) stress during one major event. The y axis is normalized time, and the x axis is distance along strike. The entire model domain is shown. The fault repeats periodically along strike, so the velocity-strengthening section (where $a > b$) wraps around the edge of the plot. The event nucleates near the velocity-strengthening section and propagates steadily "along strike" from left to right. Horizontal dashed lines indicate the times of peak applied shear stress. The slip rate is higher at these times, as indicated by the redder colors in Figure 2a. Back-propagating fronts nucleate and propagate back along strike around this time. This aging law simulation uses $a/b = 0.8$, $W/L_b = 500$, and has no low-normal-stress region. The tidal forcing has amplitude $A_t = 0.05b\sigma$ and period $T_t = 37.5D_c/V_{\tau\text{-min}}$. The x's indicate the location for which we plot stress and velocity in Figure 4.

3. Features of Large Slow Slip Events Unrelated to Tides

[17] In the simulations considered here, large events rupture the entire fault at relatively regular intervals. We plot slip rate and stress during one such event in Figure 2. Events nucleate near the region where $a > b$ and then propagate across the fault—"along strike" in the strip model—at an approximately steady rate. During this propagation, the profiles of stress, slip rate, and state are translated across the fault almost unchanged except for the effects of tidal forcing, as seen in Figure 3. We examined these profiles in detail in paper 1. In this section, we summarize a few properties that will be relevant when we discuss tidal modulation and back-propagating fronts in sections 4 and 5.

[18] To illustrate the behavior of a slow slip event, we consider the evolution of stress and velocity at a single location as slow slip events approach and rupture through it. These values at one location are plotted in Figure 4a. Before the slow slip front arrives, this part of the fault is slipping very slowly, has large initial state θ_i, and is below steady state ($V\theta/D_c < 1$). The stress and velocity plot in the lower left corner of Figure 4a, in the segment labeled 1. When the front arrives, stress increases rapidly (segment 2 in Figure 4a). The slip rate also increases rapidly in this segment, but there is little slip, so state changes by a only a small amount. Once the fault is slipping quickly, however, state evolves rapidly toward the steady state value appropriate for the new slip speed (segment 3). This decrease in state results in a decrease in stress: the peak to residual stress drop $\Delta\tau_{\text{p-r}}$. The magnitude of $\Delta\tau_{\text{p-r}}$ is, to within about 5%,

$$\Delta\tau_{\text{p-r}} \approx b\sigma\left[\log\left(\frac{V_c\theta_i}{2D_c}+1\right)-\log\left(\frac{2V_c}{V_{\max}}+1\right)\right] \qquad (6)$$

(see paper 1). Here $V_{\max}$ is the maximum velocity in the front.

[19] As noted in paper 1, it is possible to gain an increased understanding of the near-tip region by considering analytical approximations to the friction law [e.g., *Bizzarri and Cocco*, 2003; *Ampuero and Rubin*, 2008]. Elasticity considerations dictate that the propagation velocity V_{prop} is related to the maximum velocity $V_{\max}$ through

$$V_{\text{prop}} \approx \alpha V_{\max}\frac{\mu}{\Delta\tau_{\text{p-r}}} \qquad (7)$$

[e.g., *Ida*, 1973; *Shibazaki and Shimamoto*, 2007; *Ampuero and Rubin*, 2008]. Here α is a constant accounting for the form of the local slip profile. In our simulations, $\alpha \approx 0.50$–0.55 for the aging law and $\alpha \approx 0.57$–0.65 for the slip law.

[20] More than a few L_b behind the front, there is a region where the fault is near steady state. The slip rate and stress decay gradually behind the front along the velocity-strengthening section of the steady state stress-velocity curve, with $V\theta/D_c$ slightly less than 1 on average (segment 4 in Figure 4a, and Figures 4b and 4c). This region will be important when we investigate tidal modulation because about 90% of the slip accumulates here. It usually extends 0.2 to $0.5W$ behind the front. In Cascadia, where W is 50 to 100 km [*Wech et al.*, 2009; *Schmidt and Gao*, 2010], it might span 10 to 50 km along strike.

[21] At the trailing edge of the region near steady state, the slip rate falls below $V_{\tau\text{-min}}$. It is no longer possible for stress and velocity to follow the velocity-strengthening section of the steady state curve, and the fault falls below steady state (segment 5 in Figure 4a). The stress either stays the same or increases by up to 30% of the maximum

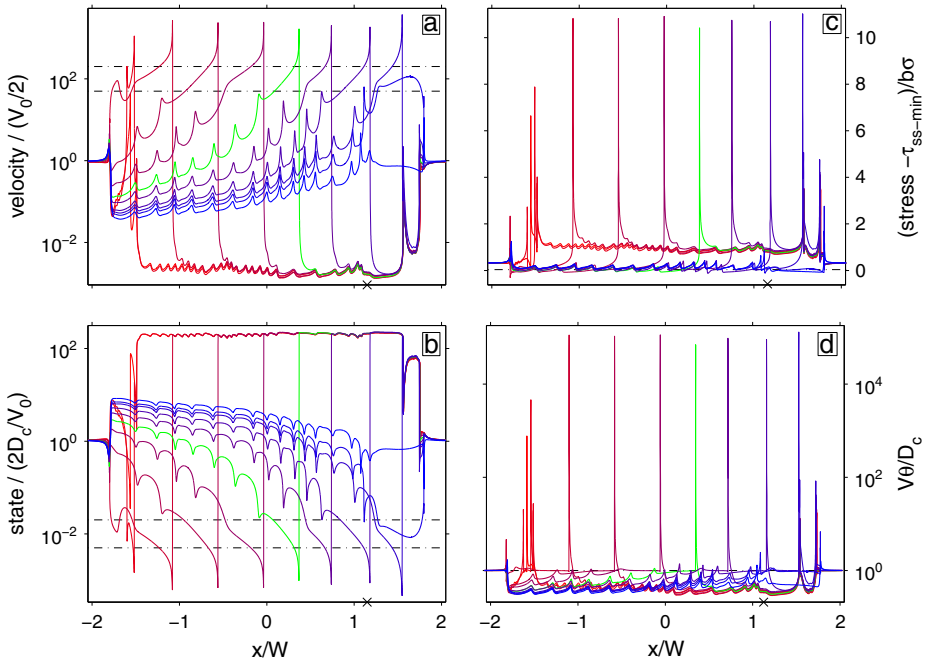

Figure 3. Snapshots of (a) velocity, (b) state, (c) stress, and (d) $V\theta/D_c$ during part of the slow slip event shown in Figures 2c and 2d. The event propagates approximately steadily "along strike" from left to right. Snapshots are approximately equally spaced in time, which progresses from red to blue. The peaks in velocity and stress behind the front come from back-propagating fronts that arise every tidal cycle. Dashed-dotted lines in Figure 3a indicate V_c (top) and $V_{\tau\text{-min}}$ (bottom). Dashed-dotted lines in Figure 3b indicate D_c/V_c (bottom) and $D_c/V_{\tau\text{-min}}$ (top). The x's indicate the location for which we plot stress and velocity in Figure 4.

stress drop. In events where stress increases, the stress in much of the region below steady state is larger than the minimum steady state stress $\tau_{\text{ss-min}}$. A region with such large stress has the potential to undergo a stress drop. It will be important in generating back-propagating fronts.

4. Quasi-Sinusoidal Modulation of the Slip Rate

[22] An examination of Figure 2 reveals two features associated with the tides. First, the slip rate on the entire fault changes approximately sinusoidally, with higher velocities (redder colors) occurring near the times of the shear stress maxima (horizontal dotted lines). Second, back-propagating fronts with relatively large slip speeds arise around the times of the tidal maxima. We will examine the back-propagating fronts in section 5. In this section, we investigate the quasi-sinusoidal modulation, which is present in all tidally forced simulations.

4.1. Gradual Modulation of a Ramp Block Slider: Effect of Tidal Period

[23] To begin our investigation, we consider the effect of tidal forcing on a simpler system: a zero-stiffness spring block slider (a block sliding down a ramp) governed by our chosen friction law. This system provides a good conceptual model for the modulation of slip rate in the simulated events. If the block is driven by a force that is constant in time, it slides at a steady rate V_{ref} whose value is determined by the driving stress. If we apply a sinusoidally varying shear stress with amplitude $\Delta\tau_t$ and period T_t, in addition to the constant stress, the velocity and state adjust so that the frictional strength (equation (1)) matches the time-variable driving stress.

[24] The responses of velocity and state to this tidal forcing depend on the chosen period, as seen by *Perfettini and Schmittbuhl* [2001], *Perfettini et al.* [2001], and *Ader et al.* [2012]. State evolves significantly only over slip distances longer than D_c, or timescales longer than D_c/V_{ref}. If the tidal period is much shorter than D_c/V_{ref}, state remains approximately constant throughout the tidal cycle. In this case, changes in frictional strength are taken up almost exclusively by changes in velocity. The slip rate reaches its peak value ($V_{\text{ref}} + \Delta V$) at the time of the maximum stress, and its amplitude is determined by

$$\Delta\tau_t = a\sigma\Delta \log\left(\frac{V_{\text{ref}} + \Delta V}{V_{\text{ref}}}\right) \approx a\sigma\frac{\Delta V}{V_{\text{ref}}}. \tag{8}$$

[25] At the other extreme, when the tidal period is long compared to the time needed for state evolution ($T_t \gg D_c/V_{\text{ref}}$), state remains close to its steady state value (D_c/V) throughout the tidal cycle. The evolution effect term in equation (1) thus decreases when the direct effect term increases. For the frictional strength to match a specified applied load, the velocity must increase more in this case than in the no-evolution case. The slip rate still peaks at the time of the maximum stress, and

$$\Delta\tau_t \approx \frac{\mathrm{d}\tau_{ss}}{\mathrm{d}\log(V)}(V_{\text{ref}})\Delta \log\left(\frac{V_{\text{ref}} + \Delta V}{V_{\text{ref}}}\right) \approx \frac{\mathrm{d}\tau_{ss}}{\mathrm{d}\log(V)}(V_{\text{ref}})\frac{\Delta V}{V_{\text{ref}}}. \tag{9}$$

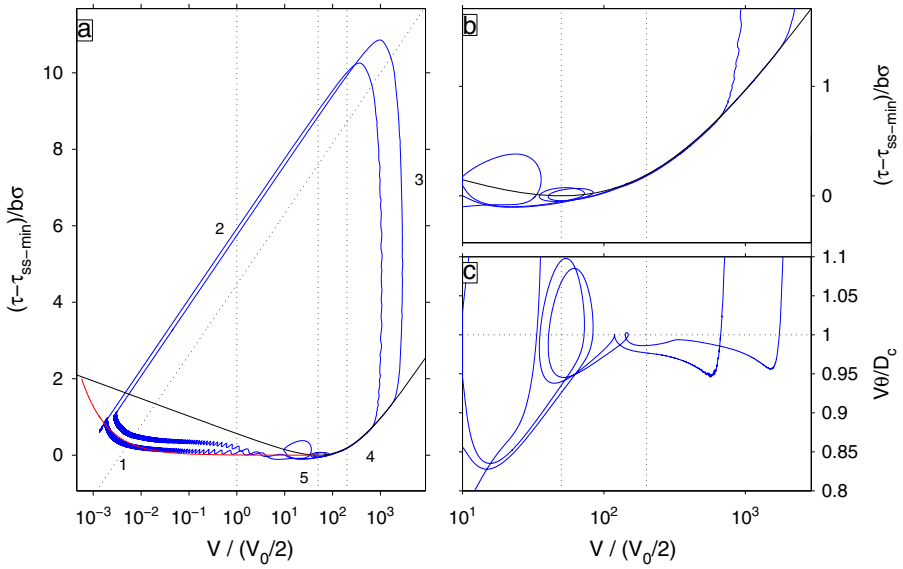

Figure 4. (a) Blue: stress versus slip rate at the location marked by an x in Figures 2 and 3. Black: steady state stress as a function of slip rate. The evolution over two slow slip events is shown. The numbers are referenced in the text. The vertical dotted lines indicate, from left to right, $V_0/2$, $V_{\tau\text{-min}}$, and V_c. The diagonal dotted line is a line of constant state. (b) Expansion of the part of the evolution in Figure 4a where this location is near steady state. Most of the slip accumulates during this interval. (c) $V\theta/D_c$ during that period. Vertical dotted lines in Figures 4b and 4c indicate, from left to right, $V_{\tau\text{-min}}$ and V_c.

Here $d\tau_{ss}/d\log V$ is the slope of the steady state stress-velocity curve. This regime is applicable only if $d\tau_{ss}/d\log V$ is positive. With the chosen friction law, $d\tau_{ss}/d\log V > 0$ when $V_{\text{ref}} > V_{\tau\text{-min}}$.

[26] At intermediate periods, the amplitude of slip rate oscillation is between the short- and long-period responses. The slip rate reaches its peak slightly after the time of the maximum stress. This delay arises because state requires a significant fraction of the tidal period to evolve to its minimum value. This implies that the evolution effect term in the frictional strength (equation (1)) reaches its minimum after the time of the maximum stress, and the direct effect term must reach its maximum later to compensate. From equation (C2) in Appendix C, we calculate that the delay in peak slip rate is smaller when $V_{\text{ref}}/V_{\tau\text{-min}}$, and thus $d\tau_{ss}/d\log V$, are larger. For $V_{\text{ref}} > 2V_{\tau\text{-min}}$, it is less than 60°.

4.2. Modulation Averaged over Multiple Events

[27] To begin our analysis of the deformable fault modulation, we examine the "average" modulation accumulated in each simulation. We bin the moment released on the part of the fault with $a < b$ by its phase in the tidal cycle throughout each simulation. We then fit a constant and a sinusoid to the log of the moment per bin, as illustrated in Figure 5a. We plot the amplitudes and phases of the best-fitting sinusoids for a number of aging law simulations in Figures 5b and 5c. Only simulations with events that last at least three tidal cycles are included.

[28] The results in Figure 5 resemble the ramp block slider results from section 4.1 in several ways. First, the phase of the tidal cycle with the most slip is usually close to the time of the maximum stress or up to one-eighth cycle later. Second, the amplitude of modulation scales approximately linearly with the forcing amplitude A_t. $A_t/a\sigma$ varies by a factor of 17 among the simulations plotted in Figure 5, but normalizing the resulting modulation by $A_t/a\sigma$ collapses the observed $\Delta V/V$ to a single clustered curve.

[29] Finally, the amplitude of modulation is close to the predicted no-evolution level $A_t/a\sigma$ (equation (8)) when the tidal period is shorter than about $3D_c/V_{\tau\text{-min}}$. It then increases as the tidal period increases. For reference, the slip rate in the region near steady state, where most of the slip accumulates, ranges from 1 to $30V_{\tau\,\text{min}}$. With such slip rates, we would expect significant oscillations in state at periods longer than $D_c/40V_{\tau\text{-min}}$ to $D_c/V_{\tau\text{-min}}$.

[30] There is significant scatter in the modulation amplitudes plotted in Figure 5. The most obvious outliers come from simulations with $A_t/a\sigma$ around 0.01 that have only a few tidal cycles per event. The large modulation results from the timing of the beginning of the events. The timing of event nucleation causes some scatter in the remaining simulations as well. Scatter in the modulation amplitude also arises because the back-propagating fronts described in section 5 sometimes contribute significantly to the modulation. Finally, additional scatter arises because the modulation depends to some extent on parameters other than $A_t/a\sigma$ and $V_{\tau\text{-min}}T_t/D_c$. We discuss some of these dependencies in section 4.4.

4.3. Quasi-sinusoidal Modulation, as a Function of Location

[31] We will now look in more detail at how the slip rate modulation varies along the fault and gives rise to the averaged modulation. Considering the effect of tidal forcing at a given location is complicated. The slip rate is changing

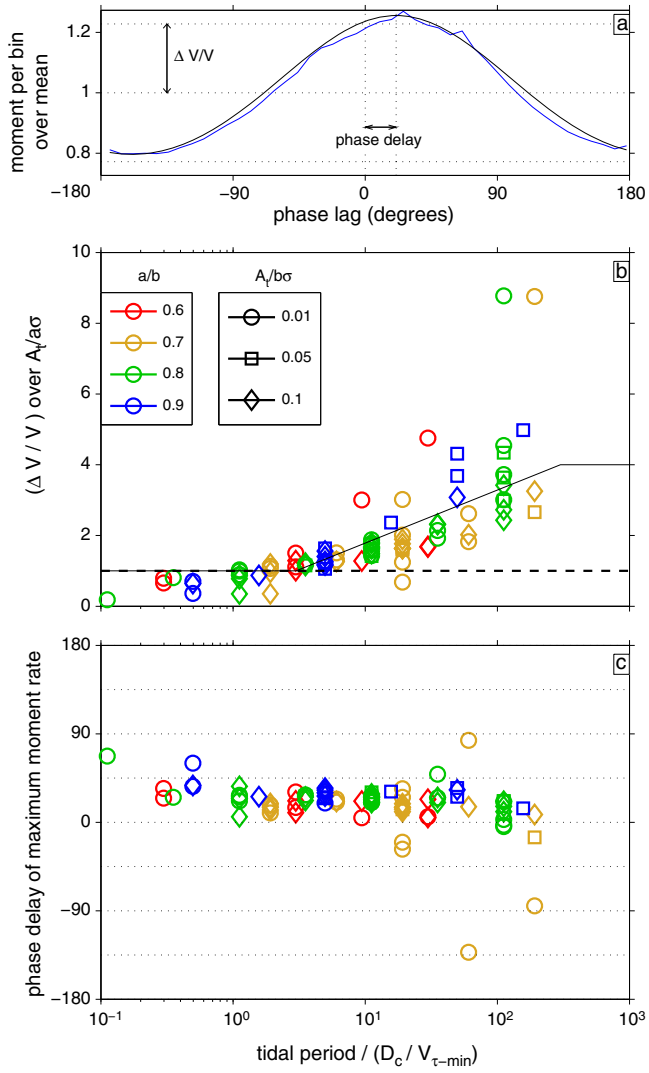

Figure 5. (a) Blue: moment accumulated throughout one simulation as a function of tidal phase, normalized by the mean value per bin. Black: best-fitting curve that varies as the exponential of a sinusoid. The arrows labeled $\Delta V/V$ and phase delay indicate the amplitude and phase of moment rate modulation that are plotted in (b) and (c), respectively. (b) Half-amplitude of moment rate modulation averaged over individual simulations, as a function of $V_{\tau\text{-min}}T_t/D_c$. Values are normalized by the expected value for no state evolution, $A_t/a\sigma$. The amplitude of modulation is close to $A_t/a\sigma$ at short periods. It is larger when $V_{\tau\text{-min}}T_t/D_c$ is larger, and the fault can remain closer to steady state during each cycle. (c) Phase delay of the averaged modulation. Zero phase is the time of the maximum applied stress, and positive values mean that the maximum moment rate occurs after the maximum applied stress. The solid black line in Figure 5a indicates the approximation we use in section 6, where we determine model parameters that can match the tidal modulation observed in Cascadia.

both because the tidal stress is changing and because this location is getting farther behind the front. In order to isolate the effect of tidal forcing, we consider a reference frame that moves with the propagating front. We plot snapshots of velocity in this reference frame in Figure 6b. The slip rates are higher near the time of the maximum tidal stress (blue and green profiles).

[32] To quantify the response of velocity to the tidal forcing, we divide the region behind the front into several bins. These are separated by the vertical dashed lines in Figure 6b. We compute the mean velocity and stress in each bin as a function of time and plot the velocity in Figure 6a. Within about $0.3W$ of the front, where the fault is near steady state, the slip rate in each bin varies approximately sinusoidally. To illustrate the relationship between the slip rate and stress in each bin, we plot the stress against the slip rate in Figure 7.

[33] Finally, we fit a constant and a sinusoid to the average slip rate in each bin. The estimated amplitudes and phases of the slip rate modulation are indicated by the red x's in Figures 6c and 6d. Similarly, we extract the periodic variation in stress by fitting a constant and a sinusoid to the average stress in each bin. The amplitudes and phases of the periodic components of stress are indicated by blue x's.

4.3.1. Modulation Near Steady State

[34] The portion of the fault that contributes the most to the moment rate modulation is the region near steady state. As seen in Figure 6, the slip rate varies approximately sinusoidally in this region, and the amplitude of that variation increases with distance behind the front. We can understand that increase qualitatively if we note that the slip rate decreases behind the front. As seen in Figure 7, the slope of the steady state stress-velocity curve $d\tau_{ss}/d\log V$ is smaller for smaller velocities. If the fault stays near steady state throughout the tidal cycle, this results in a larger modulation at smaller velocities (equation (9) and section 4.1).

[35] On the other hand, a smaller slip rate implies a smaller VT_t/D_c and therefore less slip per tidal cycle. State deviates more from its steady state value for bins farther behind the front, as seen in Figure 7. The modulation is reduced when the fault does not follow the steady state curve, as suggested by equation (8). However, in the simulation in Figure 6, and in most other simulations with $V_{\tau\text{-min}}T_t/D_c > 10$, the smaller $d\tau_{ss}/d\log V$ at low slip rates is more important than the low VT_t/D_c. The amplitude of modulation usually increases with distance behind the front.

[36] We consider the effect of changing the slip rate and VT_t/D_c more quantitatively in Appendix B. We allow sinusoidal variations in the stress, slip rate, state, and propagation velocity and solve for the changes in slip rate and state as a function of the local change in stress and $V_{\text{ref}}(x')T_t/D_c$. Here $V_{\text{ref}}(x')$ is the slip rate at a distance x' behind the front for a reference (unmodulated) profile. We find that a good approximation for the relation between the periodic components of stress and slip rate is

$$\tau_1(x') = \frac{V_1(x')}{V_{\text{ref}}(x')}\left(a\sigma - b\sigma\left(i\frac{2\pi D_c}{V_{\text{ref}}(x')T_t}+1\right)^{-1} \times \left(\frac{V_{\text{ref}}(x')\theta_0(x')}{D_c}+\frac{V_{\text{ref}}(x')}{V_c}\right)^{-1}\right). \quad (10)$$

Here τ_1 and V_1 are complex numbers whose amplitude and phase indicate the amplitude and phase of the sinusoidal variation of the stress and slip rate, respectively (see equations (B1)–(B4)).

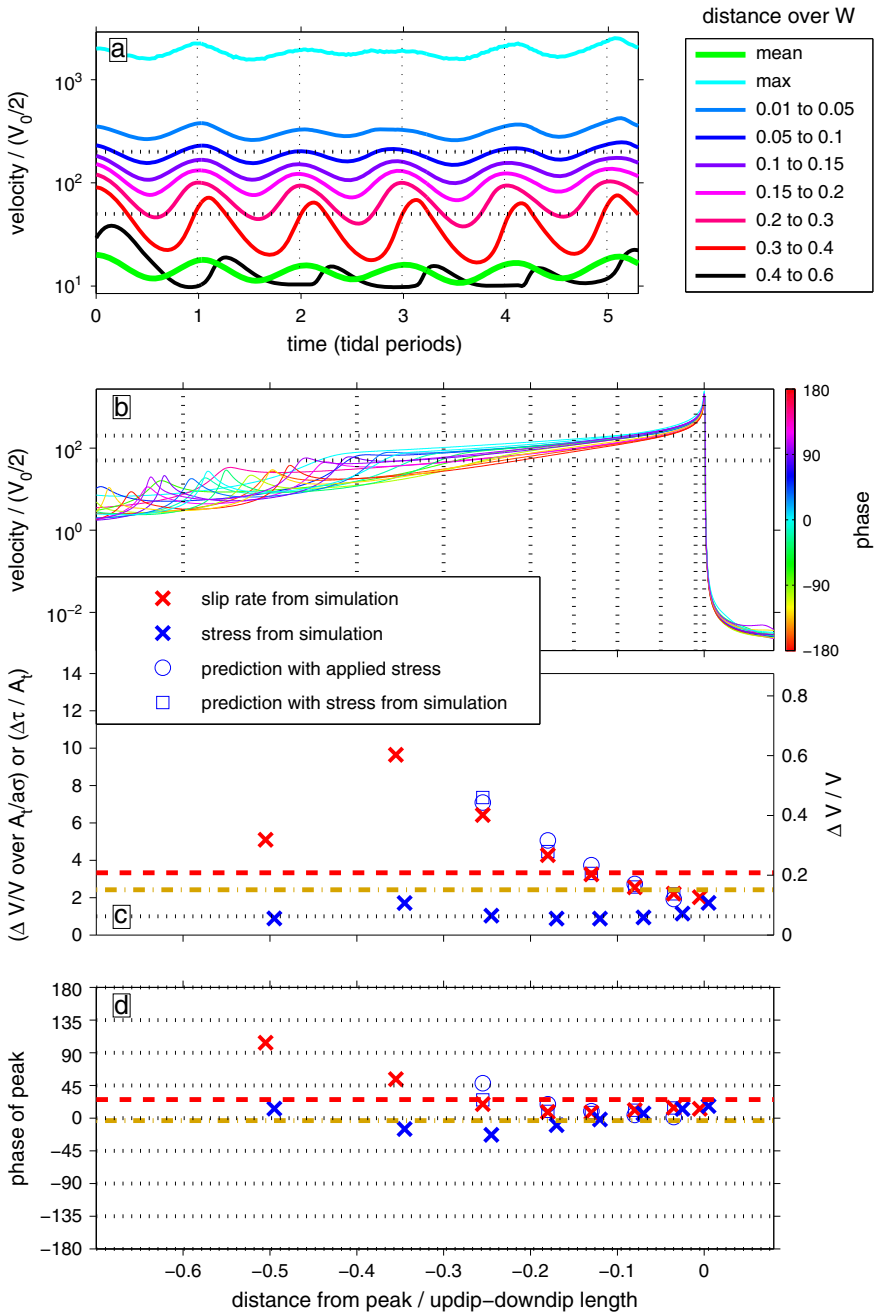

Figure 6. (a) Mean slip rates in bins behind the front over several tidal periods during part of the time interval plotted in Figure 2. The bin limits are indicated in the legend and in (b). The maximum and mean slip rates are also plotted. Vertical dashed lines indicate the times of maximum applied stress. Horizontal dashed lines in (a) and (b) indicate V_c and $V_{\tau\text{-min}}$. (b) Snapshots of slip rate over the time period in Figure 6a, shifted to align the maximum velocity. Color indicates the phase delay of each snapshot, where zero is the time of the maximum applied stress, and positive values imply times after the maximum stress. (c) Amplitude and (d) phase delay of the periodic components of velocity and stress in the bins in Figure 6b. Velocity is indicated by red x's, and stress is indicated by blue x's. Horizontal red dashed lines mark the amplitude and phase of the moment rate modulation. Tan dashed-dotted lines mark the amplitude and phase of the propagation rate modulation. Open blue circles indicate the predicted modulation of velocity in each bin given the applied tidal forcing. Open blue squares indicate the predicted modulation of velocity given the stress modulation in each bin taken from the simulation (from the blue x's), which accounts for the elastic interactions between neighboring regions.

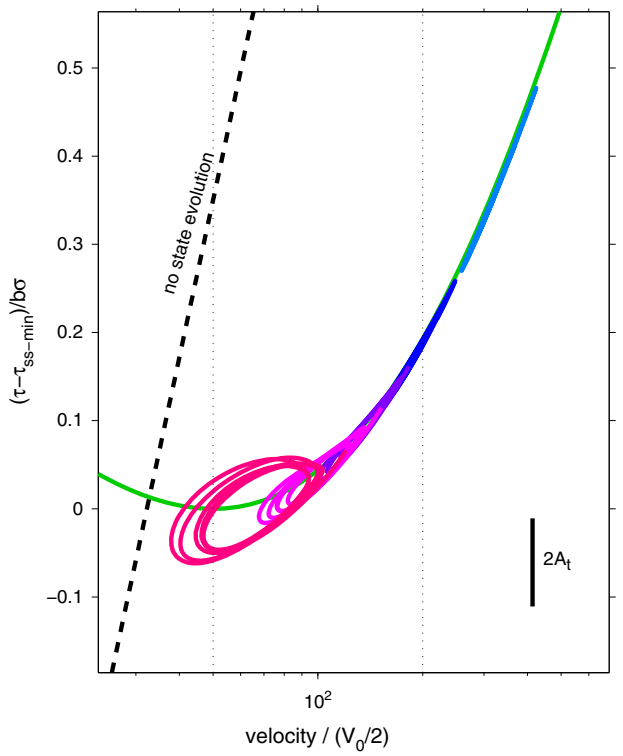

Figure 7. Colored solid curves: stress versus slip rate in bins on the part of the fault near steady state, for the simulation in Figure 6. The color for each bin is the same as in Figure 6a. Green: steady state frictional strength. At high velocities, VT_t/D_c is large, and the fault stays near steady state. At low velocities, VT_t/D_c is small, so there is not enough slip to allow for complete state evolution in each tidal cycle. If there were no state evolution, stress and velocity would move parallel to the dashed curve labeled "no state evolution." The bar labeled $2A_t$ indicates the peak to trough tidal stress.

[37] The modulation predicted by equation (10) is plotted in Figure 8. This approximation turns out to be identical to the ramp block slider modulation discussed in section 4.1 and Appendix C. To demonstrate its accuracy, we calculate the modulation predicted for each of the bins in Figure 6, assuming that the applied tidal load dominates the local variation in stress. We plot these predictions (open circles) along with the modulation extracted from the simulation (red x's) in Figures 6c and 6d. They match the simulation results reasonably well. To do a slightly better job, we can extract the periodic component of stress directly from the simulation (blue x's) and insert this stress into equation (10). The resulting prediction is indicated by the open squares in Figures 6c and 6d. The extracted stress used in this calculation includes the applied load (A_t) and any stress changes due to interacting tidally modulated slip. In this example, the two sets of predictions are not too different, as the elastic stresses due to tidally modulated slip are smaller than the applied tidal load.

[38] The predictions in Figure 8 match several features of the modulation averaged over entire events, shown in Figure 5. The magnitude of the average modulation is near $A_t/a\sigma$ at short periods and increases with increasing $V_{\tau\text{-min}}T_t/D_c$. Equation (10) predicts that the magnitude of modulation should tend to a constant at long periods. We do not see this in Figure 5. That may be because we have not run many simulations with very long periods because of computational constraints. We do find that in some simulations that plot on the right edge of Figure 5, the fault remains near steady state in the entire region with slip rates larger than $V_{\tau\text{-min}}$ throughout each tidal cycle. As near-steady-state modulation is a limiting case, it seems unlikely that quasi-sinusoidal modulation could result in much larger amplitudes.

[39] In many of the simulations plotted in Figure 5, the maximum moment rate occurs 10 to 40° after the time of the maximum applied stress. In some intermediate-period simulations, the delay relative to the maximum stress arises because state requires some fraction of the tidal cycle to evolve. More often, however, it is due to back-propagating fronts. The maximum moment rate in these fronts typically occurs slightly after the time of the maximum tidal stress. They often make significant but not dominant contributions to the modulation of the moment rate. One example of this timing can be seen in Figure 6, where the back-propagating fronts dominate the modulation in the bin between 0.3 and 0.4W.

4.3.2. Modulation Below Steady State

[40] In the event in Figure 6, the fault is below steady state more than 0.3W behind the front, with $V\theta/D_c$ typically between 0.1 and 0.7. Both back-propagating fronts and quasi-sinusoidal modulation affect the tidal changes in slip rate in this region. When $V\theta/D_c$ is this small, quasi-sinusoidal variations in the slip rate only weakly affect the rate of change of state dictated by the evolution law (equations (2) and (3)). In all simulations checked, tidally induced changes in state in the region below steady state are small compared to the changes in velocity. The no-evolution stress-velocity relation (equation (8)) is relatively accurate.

4.3.3. Elastic Interactions Due to Tidally Modulated Slip

[41] As noted in section 4.3.1 and seen in Figure 6, the fractional modulation of slip rate often varies with location behind the front. This variation creates elastic stresses, so the stress profile changes with phase in the tidal cycle. We discuss these elastic interactions in Appendix D. We find that they typically cause the maximum slip rate to occur earlier closer to the front. However, the system limits the magnitude of these interactions. When the chosen parameters favor large elastic interactions for a given spatial variation in slip rate modulation, that modulation actually becomes more uniform.

4.3.4. Modulation of the Propagation Rate

[42] In our simulations, the fractional modulation of the propagation rate is similar to or slightly smaller than the moment rate modulation. It has a similar amplitude and phase to the modulation of slip rate in the region near steady state not far behind the front. In Appendix E, we discuss how this modulation can be understood in the context of elasticity.

[43] In section 6.1, we use the results presented here to compare our models to observations of tidally modulated slip.

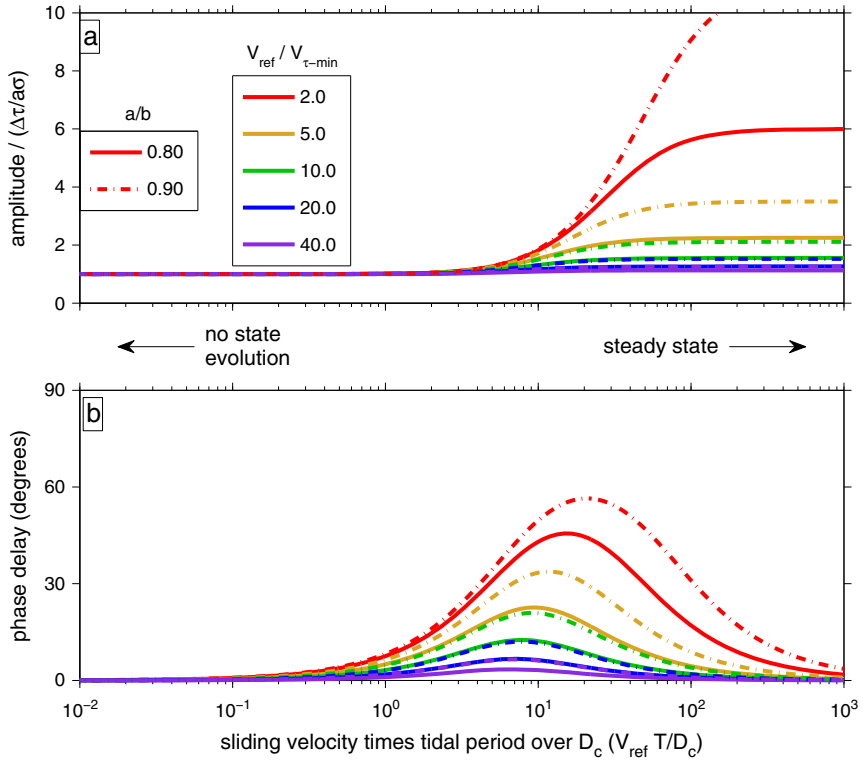

Figure 8. Predicted amplitude (a) and phase delay (b) of modulation of the slip rate from equation (10). The local stress perturbation is assumed to be a sinusoid with period T_t and amplitude $\Delta\tau$. We assume that the fault is at steady state (that $V_{\text{ref}}\theta_0/D_c = 1$). Zero phase delay is the time of the maximum stress. V_{ref} is the local reference sliding velocity. The amplitude is normalized by the expectation for no state evolution.

4.4. Modest Influence of Additional Parameters on the Modulation

[44] Figure 5b shows that the amplitude of the slip velocity modulation increases essentially linearly with normalized amplitude of the tidal load $A_t/a\sigma$ and in a systematic way with the normalized slip distance per tidal period $V_{\tau\text{-min}}T_t/D_c$. As noted in section 4.2, much of the scatter in the figure is due to the modulation of the start time of the events. We do not consider this triggering effect here. We wish to compare our results with observations of events that last many tidal cycles. In this type of event, the gradual modulation of the moment rate during the event is more important than the modulation of the event start times. We therefore do not directly investigate how the length and time scales of event nucleation affect the tidal triggering.

[45] To see that the modulation of slip speed during an event depends on parameters other than $A_t/a\sigma$ and $V_{\tau\text{-min}}T_t/D_c$, consider equation (10), which is a simplification of equation (B10). As seen in Figures 6 and D1, these equations reasonably approximate the relationship between the local periodic stress perturbation τ_1 and the modulation of slip speed $\Delta V/V_{\text{ref}}$. The local stress perturbation τ_1 is just the tidal load A_t when the elastic stress interactions due to tidally modulated slip are insignificant. Even when those interactions are significant, the average τ_1 is still close to A_t because unloading in some regions produces loading in others (Appendix D). If we replace τ_1 with A_t in equation (10) and divide by $a\sigma$, we recover a roughly linear relationship between $A_t/a\sigma$ and $\Delta V/V_{\text{ref}}$, as seen in Figure 5. This relationship also involves several other parameters: $V_{\text{ref}}T_t/D_c$, a/b, and V_{ref}/V_c. As shown in Figure 8, the modulation increases with increasing a/b and with decreasing V_{ref}/V_c. For reasons discussed in paper 1, the average V_{ref}/V_c is a factor of a few smaller in simulations with the larger a/b considered here. This would predict a slightly larger modulation for larger a/b. That may be visible in Figure 5b, but if so, the variation appears to be smaller than the scatter we attribute to the timing of the start of events.

[46] Although it is difficult to guarantee that there is no portion of parameter space where these other parameters play an important role, in the wide range of simulations we have run, the amplitude of modulation is well characterized by $A_t/a\sigma$ and $V_{\tau\text{-min}}T_t/D_c$. In particular, we note that for the simulations we have run, the amplitude of modulation seems to be better explained by considering its variation with $A_t/a\sigma$ than with the (perhaps more intuitive) $A_t/\Delta\tau$, where $\Delta\tau$ is the event stress drop.

[47] We note also that there does not appear to be a resonant or intrinsic period of oscillation in this system that can interact with the tidal loading timescale, at least during the course of an individual slow slip event. There are no quasi-periodic oscillations in slip rate in simulations without tidal forcing. There is of course the recurrence interval, analogous to the intrinsic period of a spring block slider. Interaction of this interval with the tidal period can influence the timing of event nucleation.

5. Back-Propagating Fronts

[48] The quasi-sinusoidal modulation described in section 4 is not the only change in slip rate associated with the tides. Small regions of rapid slip often develop around the time of the maximum tidal stress. These sub-events develop into fronts that propagate in the opposite direction as the main front, back through the region that has already slipped. Around 10 of these back-propagating fronts are visible in Figure 2.

5.1. Initiation

[49] In the first column of Figure 9, we plot snapshots of velocity, stress, state, and $V\theta/D_c$ before and during the growth of one back-propagating front. The snapshots span approximately one tidal cycle, from minimum to minimum. The back-propagating front initiates just before the tidal stress reaches its maximum. It occurs on the part of the fault where, at least initially, slip rates are smaller than the minimum steady state stress velocity $V_{\tau\text{-min}}$ and the stress is below steady state. The region close to the stress minimum is only slightly below steady state, however, and the tidal forcing pushes $V\theta/D_c$ in this small region to a value slightly larger than 1 (second snapshot in Figure 9d). State in this small region then decreases toward the steady state value appropriate for the new local slip rate (third snapshot in Figures 9a–9e). That evolution produces a stress drop and allows the local slip rate to increase further.

[50] The slip associated with this stress drop produces a stress concentration in the region slightly farther behind the main front and pushes that region above steady state. That location evolves to steady state and experiences a stress drop, and a back-propagating front develops, as seen in the bluer curves in Figure 9. The initial stress in the region that the back-propagating front moves through is larger than the minimum steady state stress $\tau_{\text{ss-min}}$. The final stress in a back-propagating front is typically around $\tau_{\text{ss-min}}$, so this region experiences a net stress drop. That stress drop drives the back-propagating front.

5.2. Potential Sources of Accumulated Stress

[51] The large initial stress that drives the back-propagating fronts can be achieved in several ways. First, it arises naturally in steadily propagating events. As described in section 3, stress falls to a minimum value close to $\tau_{\text{ss-min}}$ about 0.2 to 0.5W behind the front, and then it increases farther behind the front. As discussed by *Hawthorne* [2012], this stress increase, or recovery, arises because the slip rate falls off quickly once the fault falls below steady state. The region with small slip rates is loaded by the slip associated with continued propagation. In non-tidal simulations, the stress recovery ranges from near zero to around 30% of the maximum stress drop.

[52] A second component of the available stress drop comes from tidal loading. Tidal forcing results in a larger stress in the region below steady state during part of the tidal cycle. In events such as that in Figure 9, where the stress recovery is small, the direct tidal loading accounts for most of the stress drop in the back-propagating front. In other events, it is only a minor component.

[53] One final potential source of stress drop arises when the modulation of slip rate varies in space. This variation creates tidally changing elastic stresses. In Appendix D, we examine the potential for those stresses to drive back-propagating fronts. We conclude that with their timing and magnitude, they likely make only a minor contribution to the driving stress in our simulations and in real events in Cascadia.

5.3. Triggered Fronts in Simulations Without Tides

[54] The stress recovery is often the simplest and largest source of stress drop in the back-propagating fronts, but fronts rarely nucleate in simulations without tidal forcing. In order to examine what these fronts would look like if some heterogeneity did trigger nucleation, we design a set of simple simulations. Each simulation has only one main event and one back-propagating front. It begins with a uniform initial stress and state. We artificially nucleate an event at one end of the fault and allow it to propagate at least $2W$ along strike, so that it achieves steady propagation. We then gradually apply an additional load over the entire fault to trigger a back-propagating front. This load increases from 0 to A_d over a time $T_d = 10D_c/V_{\tau\text{-min}}$, with the form $A_d/2(1 - \cos(4\pi(t - t_{\text{start}})/T_d))$.

[55] This stress step pushes a small part of the fault above steady state. That region evolves to steady state, experiences a stress drop, and a back-propagating front develops as described in section 5.1. One of these triggered fronts is illustrated in Figure 10. In that simulation, the stress step A_d is 25% of the pre-existing stress recovery, so the stress recovery dominates the stress drop in the back-propagating front.

5.4. General Description

[56] Once the back-propagating front attains a maximum slip rate around $2V_{\tau\text{-min}}$, the back-propagating front resembles the forward-propagating one described in section 3. The fault is below steady state ahead of the back-propagating front. The slip rate and stress increase rapidly when the front arrives. Once the fault is slipping quickly, state decreases rapidly. The peak to residual stress drop in this region is well approximated by equation (6). The propagation velocity V_{prop} is related to the slip rate and stress change in this region through equation (7).

[57] When the maximum velocity is larger than several times $V_{\tau\text{-min}}$, the stress and velocity in the back-propagating front decay along the steady state curve for some distance behind the front, as seen in the magenta and green snapshots in Figure 10. Once the fault falls below steady state, the stress either stays the same or increases slightly, as was the case in the main front.

[58] The back-propagating fronts eventually slow and fail as they propagate back. In some cases, this failure is because the initial state is larger farther behind the main front, and the back-propagating front does not have enough energy to rupture through such a well-healed region. In tidal simulations, the front often fails as it attempts to move into a region that has low initial stress because it was ruptured by a back-propagating front in a previous tidal cycle.

5.5. Slip and Propagation Rates as a Function of Stress Drop and Initial State

5.5.1. $K = 0$ Requirement

[59] If we wish to compare the modeled back-propagating fronts with the observed tremor reversals, we need to

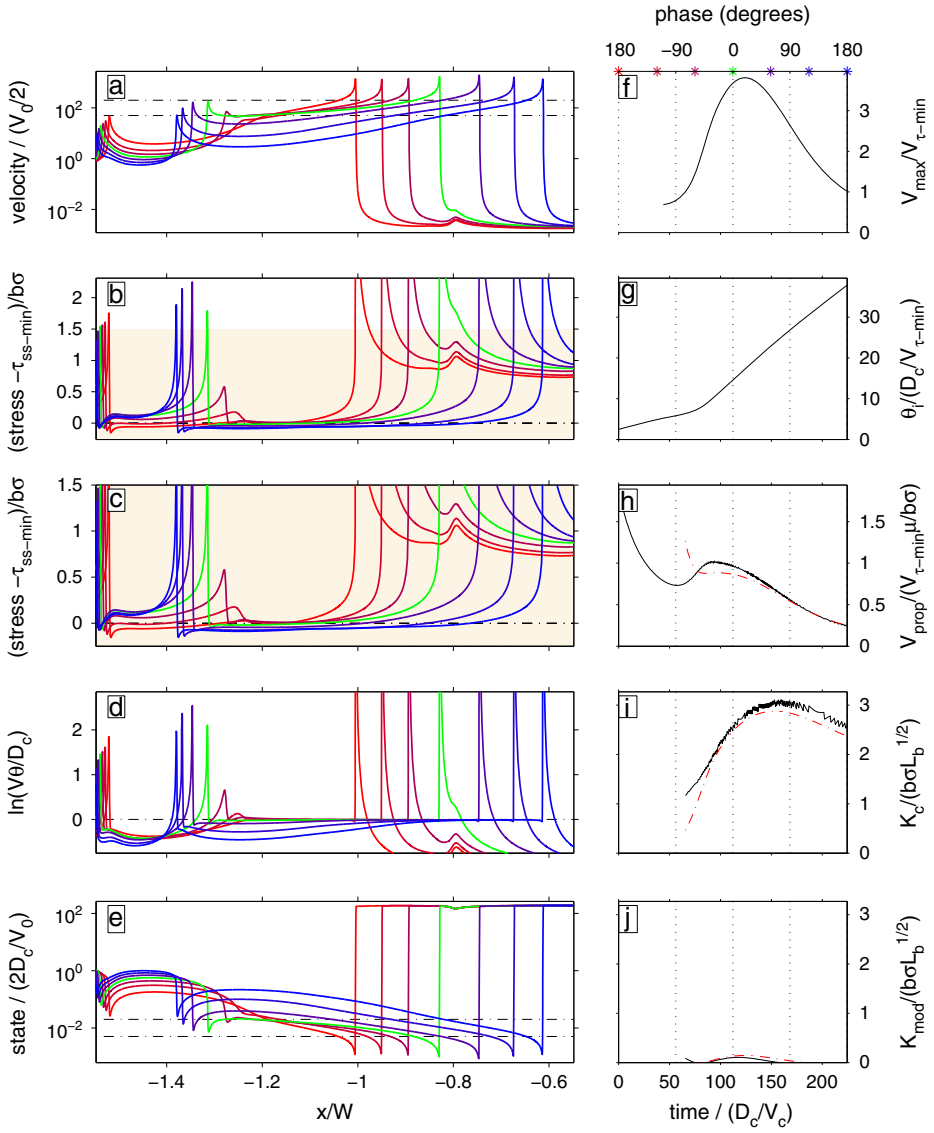

Figure 9. Snapshots of (a) velocity, (b and c) stress, (d) $V\theta/D_c$, and (e) state before and during a back-propagating front. The snapshots span roughly one tidal cycle, and time progresses from red to blue. Dashed lines in Figure 9a mark V_c (top) and $V_{\tau\text{-min}}$ (bottom). Dashed lines in Figure 9e mark D_c/V_c (bottom) and $D_c/V_{\tau\text{-min}}$ (top). (f) Maximum slip rate extracted from the back-propagating front. It is plotted only when there is a local velocity maximum. Stars on the upper axis indicate the times of the snapshots plotted in the first column. (g) Value of state 5 L_b ahead of the location of the maximum stress in the back-propagating front. (h) Black curve: propagation velocity of the back-propagating front, determined by differencing the locations of the minimum stressing rate associated with the front. Red dashed curve: propagation velocity prediction from equation (7), using $V_{\max}$ and θ_i from Figures 9f and 9g. The prediction is calculated only once $V_{\max}$ reaches $V_{\tau\text{-min}}$, since before then the front is poorly defined and the V_{prop}-$V_{\max}$ relationship in equation (7) is inappropriate. (i) Black: K_c calculated from the simulation snapshots. The jaggedness is due to numerical inaccuracies in these calculations. Red dashed: predicted K_c, using $V_{\max}$ and θ_i from Figures 9f and 9g. (j) Black: K_{mod} calculated from the simulation snapshots. We integrate contributions to K_{mod} until we reach a local stress minimum behind the front. We calculate K_{mod} only when there is a local velocity maximum and $V_{\max}$ is larger than $V_{\tau\text{-min}}$. Red dashed: K_{mod} predicted using the approximations described in the text, with $V_{\max}$ and θ_i from Figures 9f and 9g. This aging law simulation has a/b of 0.8, W/L_b of 500, no low-normal-stress region, $A_t/b\sigma$ of 0.05, and $V_{\tau\text{-min}}T_t/D_c$ of 110.

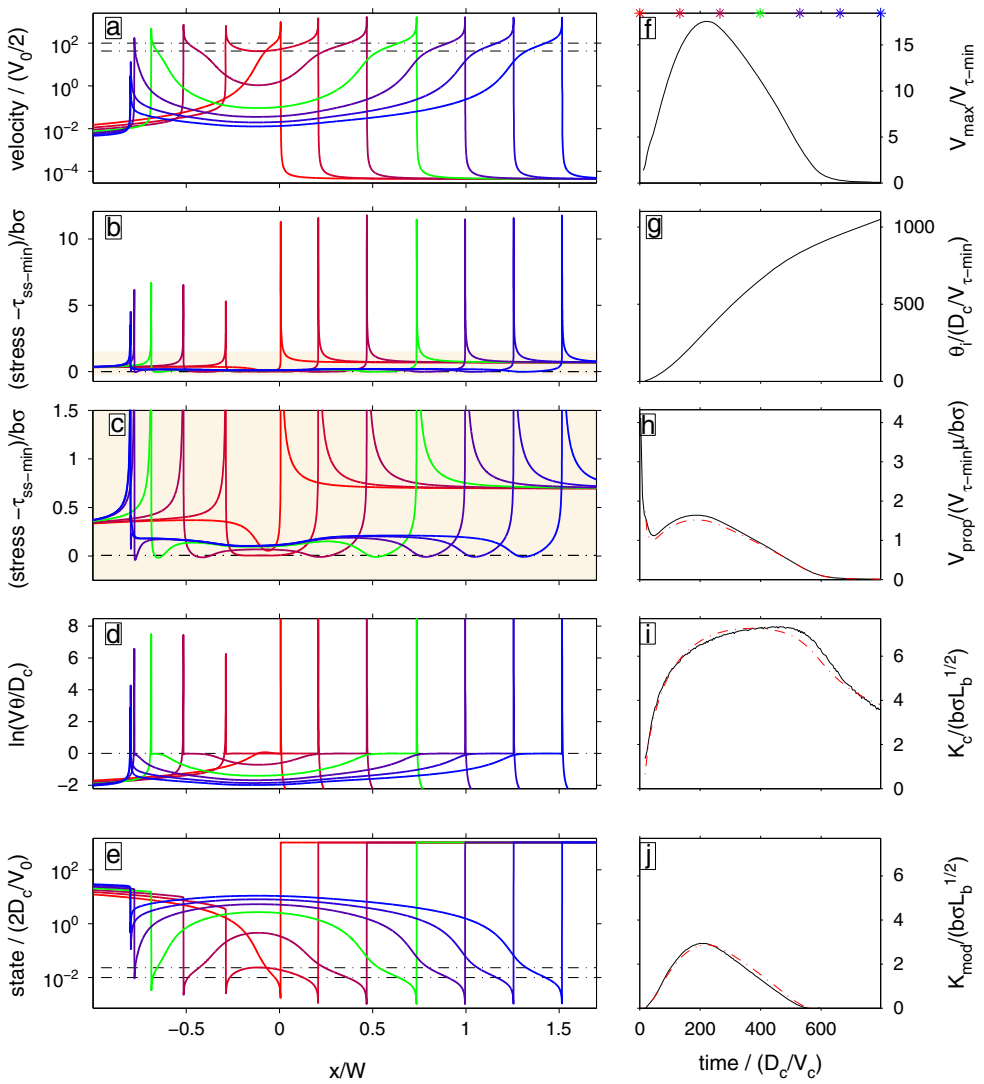

Figure 10. The same as Figure 9, but for an artificially triggered back-propagating front, starting in a steadily propagating event in a simulation without tides. The first snapshot is taken just at the end of the step in stress.

understand what controls the slip and propagation rates in the modeled fronts. To do so, we make use the stress intensity factor K, which is a measure of the potential stress singularity at the tip of the propagating rupture. If stress is to remain finite, K must be zero. The $K = 0$ requirement constrains our back-propagating fronts because K can be written as a function of the stress change behind the front:

$$K = \int_0^{L_s} c_k(x)\,(\tau_{\text{init}}(x) - \tau(x))\,\mathrm{d}x \qquad (11)$$

[e.g., *Lawn*, 1993]. Here $\tau_{\text{init}}(x)$ is the stress in the region of interest before the back-propagating front arrives. L_s is the along-strike extent of the region with nonzero slip, and x is distance behind the back-propagating front (toward the main front). $c_k(x)$ is a set of coefficients that depends on the strip model geometry and on L_s. We determine the values of $c_k(x)$ for our strip model numerically, assuming an L_s of $4W$ and a Poisson's ratio of 0.25.

[60] We divide K into three contributions, which are described and quantified in paper 1 and by *Hawthorne* [2012]. The first contribution, $K_{\Delta\tau}$, accounts for the decrease in stress from the "initial" stress τ_{init} to the final stress reached during propagation, as indicated by the blue curves in Figure 11. It is positive and can be thought of as corresponding to the strain energy released by slip. The magnitude of $K_{\Delta\tau}$ scales linearly with the stress drop in the back-propagating front. It increases as the back-propagating front grows along strike until it plateaus when the along-strike length becomes comparable to W.

[61] The remaining contributions to K are negative and can be thought of as corresponding to the fracture energy. K_c, illustrated in red in Figure 11, accounts for the high stresses in the near-tip region that is above steady state. It increases logarithmically with both the maximum velocity V_{max} and the state ahead of the front θ_i.

[62] K_{mod}, illustrated in green in Figure 11, accounts for the gradual decay of stress behind the back-propagating

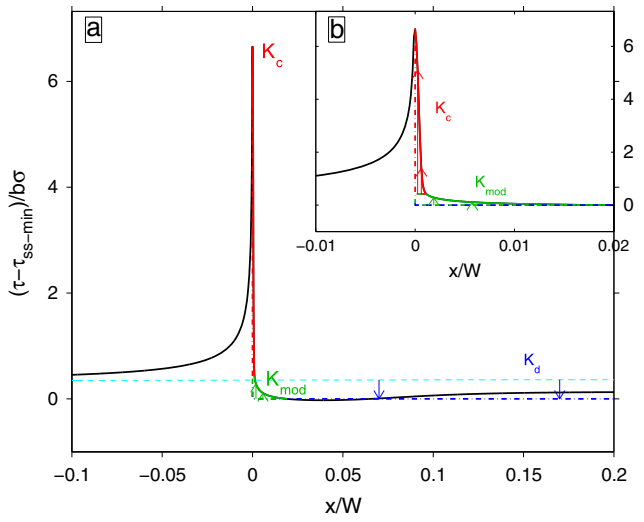

Figure 11. (a) Illustration of contributions to K in the back-propagating front. (b) Expansion of part of Figure 11a. In both panels, the combination of solid lines shows the stress profile of a back-propagating front moving to the left. The main front is off the figure to the right. Different colors indicate different contributions. Arrows originate at the reference stress used for each contribution. K_c (red) accounts for the high-stress region near the tip. K_{mod} (green) accounts for the gradual decay of stress behind the front. $K_{\Delta\tau}$ accounts for the stress drop from the initial stress to $\tau_{\mathrm{ss\text{-}min}}$ (blue dashed-dotted line). The light blue dashed line is a stress profile from before the front began.

front. It is nearly zero for V_{max} smaller than $10V_{\tau\text{-min}}$ but then increases rapidly with V_{max} at higher slip rates. For the aging law, K_{mod} is independent of the initial state θ_i. For the slip law, it decreases weakly with increasing θ_i. As will be discussed in section 5.5.2, the strong dependence of K_{mod} on V_{max} inhibits quickly propagating back-propagating fronts.

5.5.2. Allowable Slip and Propagation Rates

[63] Tremor observations indicate that back-propagating fronts move 10 to 40 times as fast as the main front [*Houston et al.*, 2011; *Obara et al.*, 2012]. In this section, we use the requirement that the positive contribution to K, $K_{\Delta\tau}$, equal the magnitude of the negative contributions, $|K_c + K_{\mathrm{mod}}|$, to determine plausible maximum and propagation velocities for our modeled fronts. On the one hand, the back-propagating fronts are driven by smaller stress drops than the forward-propagating fronts. This implies a smaller $K_{\Delta\tau}$ and thus a smaller $|K_c + K_{\mathrm{mod}}|$. When all else is constant, both $|K_c|$ and $|K_{\mathrm{mod}}|$ increase with increasing maximum velocity, so the reduced stress drop encourages smaller slip rates in the back-propagating front. On the other hand, the back-propagating fronts move into a region that is less well healed; that region has smaller initial state θ_i than the region ahead of the main front. $|K_c|$ increases logarithmically with θ_i, so the lower state encourages larger slip rates in the back-propagating fronts.

[64] When the maximum velocity is smaller than about $10V_{\tau\text{-min}}$, K_c dominates the negative contribution to K. If $K_{\Delta\tau}$, and hence K_c, is fixed, reducing θ_i by some factor increases V_{max} by approximately that factor. When the maximum velocity is larger than $10V_{\tau\text{-min}}$, K_{mod}, the contribution associated with the gradual decay of stress, becomes important. It does not decrease with decreasing θ_i. Thus, when V_{max} is larger, reducing θ_i causes a smaller increase in V_{max}.

[65] We assess the trade-off between the stress drop and θ_i more quantitatively in Figure 12. We choose two plausible values for θ_i ahead of the main front, two plausible values for θ_i ahead of the back-propagating front, and two plausible values for V_{max} in the main front: $10V_{\tau\text{-min}}$ and $30V_{\tau\text{-min}}$. The V_{max} and θ_i ahead of the main front determine its $K_c + K_{\mathrm{mod}}$ and therefore $K_{\Delta\tau\text{-forward}}$ and the stress drop driving the main front. In the first row of Figure 12, we plot V_{max} in the back-propagating front as a function of $K_{\Delta\tau\text{-back}}/K_{\Delta\tau\text{-forward}}$. If the stress drop driving both fronts were uniform and extended farther than W along strike, $K_{\Delta\tau\text{-back}}/K_{\Delta\tau\text{-forward}}$ would be equivalent to the ratio of the two stress drops. In reality, the stress drop driving the back-propagating front often extends a distance shorter than W, so the value on the x axis in Figure 12 is a lower bound on the ratio of the stress drops. We do not plot values when the predicted maximum velocity $V_{\mathrm{max\text{-}back}}$ is smaller than $2V_{\tau\text{-min}}$ because our approximations for the contributions to K break down at such low slip rates. Further, as we will see in this section and in section 6.2, fronts with such low slip rates are not good representations of the fronts observed in tremor.

[66] As seen in the second row of Figure 12, the maximum velocities in the back-propagating fronts $V_{\mathrm{max\text{-}back}}$ are typically smaller than those of the main front $V_{\mathrm{max\text{-}forward}}$, but in some cases, the two maximum velocities are comparable. However, back-propagating fronts with such high slip rates require stress drops larger than 50% of the stress drop driving the main front. We have never generated fronts with such large slip rates and stress drops in our cycle simulations. Given the potential sources of stress drop described in section 5.2, the largest plausible $K_{\Delta\tau\text{-back}}/K_{\Delta\tau\text{-forward}}$ for our simulations is 0.3 or 0.4.

[67] Next, we use the maximum velocity and initial state in the back-propagating fronts to predict their propagation rates. As noted in sections 3 and 5.4, the propagation velocities of both the forward- and back-propagating fronts obey $V_{\mathrm{prop}} \approx \alpha V_{\mathrm{max}}\mu/\Delta\tau_{\mathrm{p\text{-}r}}$ (equation (7)). The peak to residual stress drop $\Delta\tau_{\mathrm{p\text{-}r}}$ increases logarithmically with the initial state θ_i (equation (6)). For the initial states used in Figure 12, $\Delta\tau_{\mathrm{p\text{-}r}}$ is a factor of a few smaller in the back-propagating fronts than in the main fronts (Figures 12c and 12g). This reduction encourages slightly larger propagation rates in the back-propagating fronts. As seen in Figure 12d and 12h, the predicted V_{prop} ranges from much less than the forward propagation rate to around 8 times the forward propagation rate, at least for the aging law. For stress drops smaller than 50% of the stress drop driving the main front, the predicted propagation rates of the back-propagating fronts are at most twice that of the main front.

[68] When the predicted $V_{\mathrm{max\text{-}back}}$ is less than $2V_{\tau\text{-min}}$, nothing is plotted in Figure 12. The lack of values on the left half of the plot then suggests that well-developed back-propagating fronts cannot exist if $K_{\mathrm{d\text{-}back}}/K_{\mathrm{d\text{-}forward}}$ is less than 0.3. However, the fronts can nucleate. The results in Figure 12 are irrelevant during the formation of a back-propagating front, as our estimates of K_c and K_{mod} are not accurate during nucleation. Back-propagating fronts form

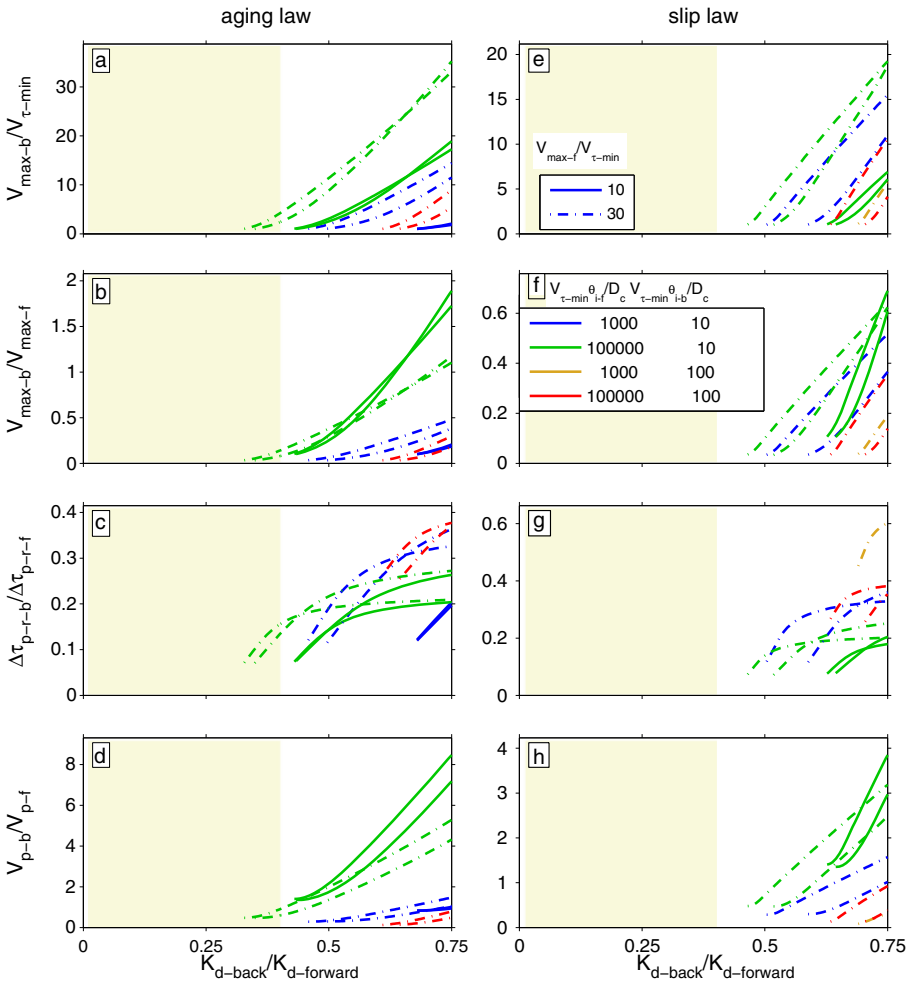

Figure 12. (a) Predicted maximum slip rate in the back-propagating front as function of the available positive contribution to K, $K_{\Delta\tau}$. Line style indicates the maximum velocity in the forward-propagating front, and color indicates the values of state ahead of the forward-propagating front and ahead of the back-propagating front. Each pair of curves is for a/b = 0.7 and a/b = 0.9. For all curves, W/L_b is 500, but this choice does not significantly influence the results. The yellow-shaded region in all panels illustrates the range of stress drops that seem plausible given the stress recovery in the simulations and the magnitude of the tidal load in Cascadia. (b) V_{max} in the back-propagating front as a fraction of that in the forward-propagating front. (c) Predicted peak to residual stress drop in the back-propagating front, as a fraction of that in the forward-propagating front. (d) Predicted propagation velocity of the back-propagating front, as a fraction of that of the forward-propagating front. (e–h) The same as Figures 12a–12d, but for the slip law. Note the difference in scale between the two columns.

every tidal cycle in many simulations, even if the available stress drop is small. They often achieve maximum slip rates of just 1 or 2 times $V_{\tau\text{-min}}$ before they begin to die.

6. Comparison With Observations

6.1. Tidal Modulation

[69] We now compare the amplitude and timing of the modeled quasi-sinusoidal modulation of slip rate with observations of tidal modulation of slow slip and tremor. First, we note that in the model, the maximum slip rate is reached at or slightly after the time of the maximum stress. This is consistent with the average timing of tremor in Cascadia [*Lambert et al.*, 2009; *Klaus*, [2011] and on the San Andreas [*Thomas et al.*, 2009, 2012]. It is also consistent with the phase of the maximum slow slip rate in Cascadia [*Hawthorne and Rubin*, 2010], although given uncertainties in the data, the slow slip moment rate in Cascadia may peak up to 90° before the maximum shear stress. *Nakata et al.* [2008] found that the tremor rate in Shikoku peaked between the maximum Coulomb stressing rate and the maximum Coulomb stress. Our model is inconsistent with that timing.

[70] *Thomas et al.* [2012] found that the first event in groups of LFEs on the San Andreas occurred more commonly near the time of the maximum shear stress. They suggested that this preferred timing was caused by a mod-

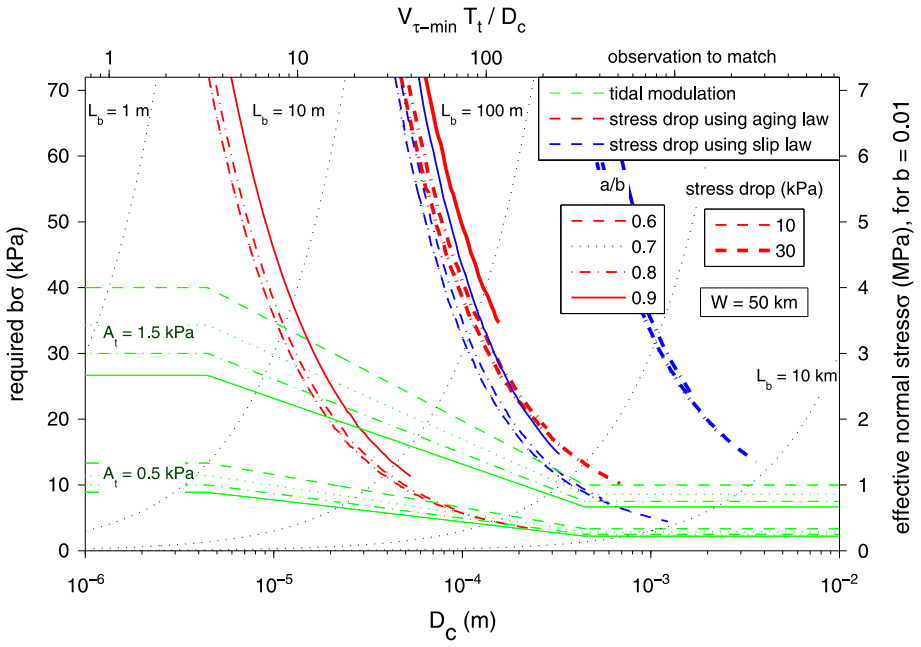

Figure 13. Required $b\sigma$ to match the observed modulation and stress drops as a function of D_c. Green curves show the parameter values required to match 25% modulation of the moment rate with the quasi-sinusoidal modulation in our models. Red and blue curves show the parameter values required to match the indicated stress drops with the aging and slip laws, respectively. Note that the results for a/b of 0.6 and 0.7 plot almost on top of each other. These curves terminate at the lower right corner when W/L_b becomes too small to allow for periodic large events. Note that curves with different a/b terminate at different locations. W is assumed to be 50 km. Sets of parameters that can match both observations can be found at the intersections of the appropriate curves. Black dotted curves are contours of L_b. To match the localization of tremor in Cascadia, L_b should be no more than to a few tens of kilometers.

ulation of the propagation rate of slow slip events. As discussed in Appendix E, that timing is consistent with the modeled modulation of V_{prop}.

[71] Next, we assess whether our model can reproduce the amplitude of moment rate modulation in Cascadia. *Hawthorne and Rubin* [2010] found that the moment rate was, on average, 25% larger than the mean during the favorable portion of the 12.4 h tidal cycle, with a 90% uncertainty of about 10% around that estimate. They calculated that the half-amplitude of the tidal shear stress (A_t) driving that increase ranges from 0.5 to 1.5 kPa, depending on location. In our models, the amplitude of modulation ranges from $A_t/a\sigma$ at periods that are short relative to $D_c/V_{\tau\text{-min}}$ to about $4A_t/a\sigma$ at periods that are long relative to $D_c/V_{\tau\text{-min}}$. For the simulated modulation to be 25%, $a\sigma$ must be between about 2 and 25 kPa. In laboratory friction experiments, a is of order 0.01 [e.g., *Marone*, 1998]. The 25% modulation then implies effective normal stresses between 0.2 and 3 MPa.

[72] The larger allowable values of $a\sigma$ correspond to larger assumed tidal loads and to larger values of $V_{\tau\text{-min}}T_t/D_c$. The strongest tidal response in Cascadia is at a period of 12.4 h, or about 4×10^4 s. Average slip rates are around 10^{-7} m/s, [e.g., *Wech et al.*, 2009; *Bartlow et al.*, 2011; *Dragert and Wang*, 2011], so a plausible $V_{\tau\text{-min}}$ is a few times 10^{-8} m/s. D_c in laboratory experiments is typically 1 to 100 μm [e.g., *Marone*, 1998]. With these values, a plausible range of $V_{\tau\text{-min}}T_t/D_c$ is between 10 and 1000. The simulation results in Figure 5 span nearly this range.

[73] In Figure 13, we illustrate the combinations of D_c, $b\sigma$, and a/b that would allow the model to match the observed modulation (green curves). Note that some of the considered D_c's are outside of the lab range. To simplify the calculation, we approximate that the modeled amplitude of modulation is $A_t/a\sigma$ for $V_{\tau\text{-min}}T_t/D_c \leq 3$, $4A_t/a\sigma$ for $V_{\tau\text{-min}}T_t/D_c \geq 300$, and that it increases linearly with $\log(V_{\tau\text{-min}}T_t/D_c)$ between these values. This approximation is illustrated with the black lines in Figure 5. We assume a tidal period T_t of 12.4 h and a $V_{\tau\text{-min}}$ of 3×10^{-8} m/s. The most uncertain part of our approximation to the simulation results is the assumption that the modulation stops increasing with $V_{\tau\text{-min}}T_t/D_c$ when $V_{\tau\text{-min}}T_t/D_c$ exceeds 300. However, this part of parameter space, which corresponds to small D_c, does not appear to be relevant for comparisons to real events, as will be seen shortly.

[74] If our model is to be a realistic representation of observed events, the set of parameters that reproduces the observed tidal modulation must also reproduce the observed stress drops. In paper 1, we showed that with the strip model geometry, the stress drop is controlled by the requirement that the strain energy released during the event be large enough to overcome the frictional energy dissipation. In other words, the positive contribution to K associated with the stress drop must be large enough to overcome the negative contributions K_c and K_{mod} associated with the transition from "static" to "kinetic" friction. Geodetic observations constrain the strain energy release rate, or the positive contributions, to K. Since $K = 0$, they also constrain the negative contributions. As discussed in paper 1, this constraint roughly determines $b\sigma D_c$ for this model, though it does not determine $b\sigma$ or D_c independently.

[75] Estimates of K_c made with the slip and aging laws differ somewhat because of how stress in the near-tip region varies with the maximum velocity and initial state [e.g., *Rubin and Ampuero*, 2005; *Ampuero and Rubin*, 2008]. Where the two laws differ in this variation, rock friction experiments support the slip law [*Ruina*, 1980; *Bayart et al*., 2006; *Ampuero and Rubin*, 2008]. The slip law is therefore our preferred evolution law when determining the parameters required to match the stress drop observations.

[76] We use the stress drop model from paper 1 to determine the combinations of $b\sigma$ and D_c that can match observed stress drops of 10 or 30 kPa and an along-dip length W of 50 km. We plot the results along with the $b\sigma$ required to match the tidal modulation in Figure 13. A W of 50 to 100 km is suggested by geodetic observations [e.g., *Wech et al*., 2009; *Schmidt and Gao*, 2010]. *Schmidt and Gao* [2010] report stress drops between 10 and 100 kPa, with an apparent clustering around 30 kPa. Stress drops are between 5 and 30 kPa if we assume a uniform stress drop along dip and if the shear modulus μ is 30 GPa, Poisson's ratio is 0.25, and events have 2 to 3 cm of slip and along-dip extents of 50 to 100 km.

[77] Additional observations further constrain the plausible part of parameter space. In the right-hand corner of Figure 13, D_c and L_b are large, and W/L_b is small. In paper 1, we show that simulations in this regime do not exhibit large periodic events like those observed in Cascadia, so we terminate the stress drop curves when W/L_b becomes smaller than the minimum required for episodic events. A second constraint that excludes the lower right corner of Figure 13 is the size of L_b, which is a length scale for localization of rapid slip [e.g., *Dieterich*, 1992; *Rubin and Ampuero*, 2005]. We do not expect large variations in slip rate on length scales much smaller than L_b for the aging law and smaller than $L_{b/10}$ for the slip law. Tremor has been observed to be concentrated on length scales shorter than 10 km [e.g., *Ghosh et al.*, 2010a, 2010b], so it seems unlikely that L_b is much more than a few to a few tens of kilometers.

[78] Parameters that match both the stress drop and tidal modulation observations can be obtained from the intersections of the appropriate curves in Figure 13. For the aging law, it is possible to choose parameters that match both the observed 25% tidal modulation and a stress drop of 10 kPa using a tidal half-amplitude of 0.5 or 1.5 kPa. Matching a 30 kPa stress drop is possible with the aging law if A_t is slightly more than 1.5 kPa, but only if $a/b \lesssim 0.8$. With the slip law, matching a 10 kPa stress drop requires an A_t slightly more than 0.5 kPa. It also requires D_c to be in a rather narrow range, between 200 μm and 1 mm. It is not possible to match a stress drop of 30 kPa and 25% tidal modulation with the slip law, even if A_t is 1.5 kPa.

[79] With these constraints, if we use the slip law—the preferred evolution law for estimating the stress drops—and require that our model reproduce the observed tidal modulation, it can reproduce only a subset of the stress drops that have been reported or seem plausible for Cascadia. Before concluding that the chosen friction law is inadequate, however, we should note two uncertainties. First, if $V_{\tau\text{-min}}T_t/D_c$ is large, the tidal forcing causes the stress and slip rate in the propagating front to move along the steady state stress-velocity curve (section 4.3.1). We have chosen one form of the steady state curve that is consistent with theoretical models (equation (1)), but this form is not well constrained by experiments. If the velocity-strengthening section of the steady state stress-velocity curve were shallower, the tidal modulation at long periods would be larger. This would not necessarily reconcile the observations with the model, however. Changing the steady state curve changes the modulation at large $V_{\tau\text{-min}}T_t/D_c$, on the left side of Figure 13. It would not change the values on the right side of Figure 13, which seem to be more relevant when comparing with the observations.

[80] A second uncertainty is that the estimates of tidal modulation given in this section are based only on the quasi-sinusoidal modulation of the slip rate. Back-propagating fronts frequently contribute to the summed modulation of slip. We have observed only a few simulations where they dominate the modulation, but their inclusion can allow for larger modulation than that predicted here. However, the back-propagating fronts observed in Cascadia are not obviously tidally modulated [*Houston et al*., 2011], so it seems unlikely that they would contribute a large fraction of the observed moment rate modulation.

6.2. Back-Propagating Fronts

[81] Back-propagating fronts in real slow slip events have been inferred from observations of tremor that moves back through the region that has already slipped. These rapid tremor reversals (RTRs) typically last 1 to 10 h and propagate 30 to 70 km at speeds around 10 to 40 times the forward propagation rate [*Houston et al*., 2011; *Obara et al*., 2012].

[82] The back-propagating fronts in our simulations last a fraction of a tidal cycle, like the observed fronts. However, they propagate too slowly to match the observations. In section 5.5.2, we found that the modeled fronts could propagate more than 2 times faster than the forward-propagating front only if the stress drop driving the back-propagating front was more than 0.5 times that driving the main front. Such stress drops seem larger than the available driving stresses. In our cycle simulations, the stress rarely recovers by more than 30% of the maximum stress drop. The direct tidal load, the other important source of driving stress, is only about one tenth of the total observed stress drops in Cascadia [e.g., *Hawthorne and Rubin*, 2010; *Schmidt and Gao*, 2010].

[83] As discussed in section 5.5.2, the modeled back-propagating fronts require these large stress drops to obtain high slip and propagation rates in part because K_{mod}, the negative contribution to K associated with the gradual decay of stress, depends strongly on the maximum slip rate and almost not at all on the initial state. The magnitude of K_{mod} depends on how stress decays behind the front and therefore on the form of the steady state stress-velocity curve. One might imagine that changing the slope of the steady state curve would allow for faster back-propagating fronts. However, as discussed by *Hawthorne* [2012], such a change may decrease the stress drop available for the back-propagating fronts and cause large variations in the forward propagation rate that are not suggested by observations.

[84] The modeled back-propagating fronts originate at the location of the stress minimum, where the fault has recently fallen below steady state. That stress minimum is typically 0.2 to 0.5W behind the front. In Cascadia, 0.2 to 0.5W is 10 to 50 km, and in Japan, it is 5 to 20 km. It can be

difficult to precisely identify the starting location of the back-propagating fronts in tremor observations, but in some cases, the tremor reversals seem to originate closer to the main front [*Obara*, 2010; *Houston et al*., 2011; *Obara et al*., 2012].

[85] When back-propagating fronts arise in tidally forced cycle simulations, they occur every tidal cycle. This periodic repetition seems consistent with some observed fronts [*Obara*, 2010] but not with others [*Houston et al*., 2011; *Obara et al*., 2012]. Even the periodically repeating observed fronts differ from the modeled fronts in their spatial extent. They rupture more than 50 km along strike [*Obara*, 2010]. The modeled tidally triggered fronts fail when they reach regions that have already hosted a back-propagating front, so their maximum length is the distance propagated by the main front in a single tidal cycle. In Shikoku and Cascadia, that distance is less than 10 km.

[86] Modeled back-propagating fronts that are driven by stress recovery can propagate much longer distances. However, each of these fronts releases most of the recovered stress, so it is unlikely that a single region could be ruptured multiple times. If a second event did occur, it would be driven by a smaller stress drop, and the slip and propagation rates would be smaller. Tremor reversals sometimes repeatedly move through a region during a single slow slip event, and the later RTRs are not obviously slower than the first [*Obara*, 2010; *Obara et al*., 2012].

[87] With the chosen friction law, for the back-propagating fronts to propagate faster than the main front, they must be driven by stress drops comparable to that of the main front. Such stress drops could exist if there were large amounts of heterogeneity in the material properties on the plate interface. Indeed, *Luo and Ampuero* [2011] modeled slow slip events using this friction law along with patches that generated seismic slip. They were able to produce back-propagating fronts that traveled about 5 to 10 times as fast as the forward-propagating front.

[88] Alternatively, the chosen friction law may not be the correct law to use when modeling slow slip. One different option is a more complicated friction law such as that used by *Rubin* [2011]. That law was designed such that for a given maximum velocity, back-propagating fronts had smaller fracture energy than the main front. This allowed back-propagating fronts to propagate rapidly despite having small stress drops.

7. Conclusions

[89] We have investigated tidal modulation and back-propagating fronts in slow slip events simulated using a strip model geometry and a friction law that is steady state velocity weakening at low slip speeds and velocity strengthening at high slip speeds. With this friction law, tidal forcing results in a quasi-sinusoidal modulation of the slip rate behind the propagating front. When the tidal period is short relative to $D_c/V_{\tau\text{-min}}$, this modulation occurs with little modulation of state, and the amplitude of modulation is around $A_t/a\sigma$. As the tidal period increases relative to $D_c/V_{\tau\text{-min}}$, there is enough slip during each tidal cycle that state can evolve significantly as the slip rate changes, and the fault remains close to steady state. When the tidal period is much longer than $D_c/V_{\tau\text{-min}}$, the stress and velocity vary along the velocity-strengthening section of the steady state curve, and the amplitude of modulation reaches 4 to $5A_t/a\sigma$. At both long and short tidal periods, the slip rate peaks at the time of the maximum tidal stress. At intermediate periods, the slip rate can peak up to 60° after the maximum tidal stress.

[90] If we use the aging law for state evolution, it is possible to choose sets of parameters that allow our model to simultaneously match the observed tidal modulation in and the observed stress drops in Cascadia. If we use the slip law, the preferred evolution law for estimating the stress drops in this model, the model can reproduce only the lower range of stress drops inferred from observations, and only if $b\sigma$ and D_c fall within a limited range. The required D_c is larger than values commonly inferred from laboratory experiments.

[91] The tidal forcing often triggers back-propagating fronts. These fronts are driven either by the tidal load or by the stress recovery that exists independently of tidal forcing. They nucleate in the region where the velocity has just fallen below $V_{\tau\text{-min}}$ and propagate back through the region below steady state. We estimate the maximum and propagation velocities in the back-propagating fronts by using the requirement that stress remains finite at the tip of propagating ruptures. The modeled fronts do not seem to be a reasonable representation of the fronts inferred from tremor observations. They require implausibly large stress drops to reach the observed propagation rates, and unlike some of the fronts observed in tremor, they do not repeatedly rupture a single region. If this friction law is the appropriate constitutive law for slow slip, the back-propagating fronts must have large stress drops. Heterogeneity on the fault surface could help facilitate such stress drops.

Appendix A: Model Setup Details

[92] As noted in section 2.3, we introduce some variations in a/b and normal stress in our modeled faults. There is a region with width of $0.5W$ which obeys equation (1) but has $a > b$. b in this region is the same as it is on the rest of the fault, but $a - b$ here is equal to $b - a$ elsewhere. The normal stress in this purely velocity-strengthening section is a factor of 10 larger than on the rest of the fault. With these parameter choices, the region with $a > b$ slips at a nearly steady rate during and between simulated slow slip events. This steady slip loads the adjacent regions and allows for nucleation of slow slip events, as described in paper 1. To further encourage frequent nucleation, in some simulations we reduce the normal stress in the velocity-weakening region within 0.125 or $0.25W$ of the region with $a > b$ to 0.1 or 0.3 times that on the bulk of the fault.

[93] We run our simulations using dimensional terms. In all simulations, the downdip loading rate V_0 is 10^{-9}m/s (∼3cm/yr) and V_c is 10^{-7}m/s. The evolution effect parameter b is 0.01, and D_c is 10^{-5} m everywhere. The normal stress σ is 1 MPa on the bulk of the fault, the shear modulus μ is 30 GPa, and Poisson's ratio ν is 0.25. However, we describe our results in terms of the model parameters, not the physical values. *Hawthorne* [2012] normalized the governing equations and showed that keeping b, σ, and D_c constant does not restrict the portion of parameter space we explore. One set of free parameters that fully determines the model results is a/b, ν, W/L_b, L/W, V_0/V_c, $A_t/b\sigma$, and V_cT_t/D_c.

Appendix B: Modulation of a Propagating Front

[94] In the simulations, state and velocity in the propagating front vary as a result of the tidal stress. In this section, we seek an approximate relationship between the periodic components of stress and velocity in the region near steady state. We will account for both the friction law and the propagation of the front. To do so, we assume that the slip rate, stress, state, and propagation velocity vary sinusoidally at the tidal period, as in *Perfettini et al*. [2001]. We write the slip rate, stress, and state in the reference frame of the moving front:

$$\tau(x',t) \approx \tau_0(x') + \mathrm{Imag}\left[\tau_1(x')e^{i\omega t}\right] \quad \text{(B1)}$$

$$V(x',t) \approx V_{\mathrm{ref}}(x') + \mathrm{Imag}\left[V_1(x')e^{i\omega t}\right] \quad \text{(B2)}$$

$$\theta(x',t) \approx \theta_0(x') + \mathrm{Imag}\left[\theta_1(x')e^{i\omega t}\right] \quad \text{(B3)}$$

$$V_{\mathrm{prop}}(t) \approx V_{p0} + \mathrm{Imag}\left[V_{p1}e^{i\omega t}\right]. \quad \text{(B4)}$$

Here t is time and $\omega = 2\pi/T_t$. x' is distance in the direction of propagation, shifted so that x' is always zero at the location of the stress peak. We insert the expansions in equations (B1)–(B3) into the expression for frictional strength (equation (1)) and obtain

$$\tau_0(x') + \tau_1(x')e^{i\omega t} \approx f^*\sigma + a\sigma\log\left(\frac{V_{\mathrm{ref}}(x')}{V^*}\right) + a\sigma\frac{V_1(x')}{V_{\mathrm{ref}}(x')}e^{i\omega t} + b\sigma\log\left(\frac{V_c\theta_0(x')}{D_c}+1\right) + b\sigma\frac{V_c\theta_1(x')}{V_c\theta_0(x')+D_c}e^{i\omega t}. \quad \text{(B5)}$$

Here we have used a first-order expansion for the logarithmic terms in the frictional strength. This is accurate to within 10% for fractional changes of up to 50%. That seems acceptable, as we are interested only in slip rate modulation of a few tens of percent. The reference profile must also obey the friction law, so the unmodulated terms in equation (B4) fall out and we are left with

$$\tau_1(x') \approx a\sigma\frac{V_1(x')}{V_{\mathrm{ref}}(x')} + b\sigma\frac{V_c\theta_1(x')}{V_c\theta_0(x')+D_c}. \quad \text{(B6)}$$

[95] This gives us a simple relation between the changes in stress, velocity, and state, but we would like to know how much velocity changes in response to stress, not in response to stress and state. The evolution laws give the temporal derivative of state, $d\theta/dt$. The region of interest is near steady state, so $V\theta/D_c$ is close to 1. When we insert the constant and periodic terms into the aging law (equation (2)) or the slip law (equation (3)) and again keep only the first-order terms,

$$\frac{\mathrm{d}}{\mathrm{d}t}(\theta_0 + \theta_1 e^{i\omega t}) \approx \left(1 - \frac{V_{\mathrm{ref}}\theta_0}{D_c}\right) - e^{i\omega t}\frac{V_{\mathrm{ref}}\theta_1}{D_c} - \frac{V_1\theta_0}{D_c}e^{i\omega t}. \quad \text{(B7)}$$

The rate of change of state given by the evolution laws is the full local derivative. It can be divided into a term for propagation and a term for the change in the state profile:

$$\frac{\mathrm{d}\theta(x')}{\mathrm{d}t} = \frac{\partial\theta(x')}{\partial t} + V_{\mathrm{prop}}\frac{\partial\theta(x')}{\partial x'}. \quad \text{(B8)}$$

Here V_{prop} is positive in the direction the front moves. When we write this equation in terms of the steady and periodic components and discard second-order terms,

$$\frac{\mathrm{d}\theta}{\mathrm{d}t} \approx i\omega\theta_1 e^{i\omega t} + V_{p0}\frac{\partial\theta_0}{\partial x} + V_{p0}\frac{\partial\theta_1}{\partial x}e^{i\omega t} + V_{p1}\frac{\partial\theta_0}{\partial x}e^{i\omega t}. \quad \text{(B9)}$$

Now we can equate the expressions in equations (B9) and (B7). The terms with no time dependence cancel, and we are left with only the periodic components. When we isolate θ_1 as much as possible,

$$\theta_1 \approx -\left(i\omega + \frac{V_{\mathrm{ref}}}{D_c}\right)^{-1}\left(\frac{V_1\theta_0}{D_c} + V_{p1}\frac{\partial\theta_0}{\partial x} + V_{p0}\frac{\partial\theta_1}{\partial x}\right). \quad \text{(B10)}$$

The first term in the second set of parentheses is the V_1-θ_1 relation expected from the evolution law if there were no propagation. The second and third terms account for advection of the periodic components of the state profile.

[96] We insert the entire expression into the frictional strength equation (B6) and simplify to obtain

$$\tau_1 \approx \frac{V_1}{V_{\mathrm{ref}}}\left(a\sigma - b\sigma\frac{V_c}{V_c\theta_0 + D_c}\left(i\omega + \frac{V_{\mathrm{ref}}}{D_c}\right)^{-1}\right) - b\sigma\frac{V_c}{V_c\theta_0 + D_c}\left(i\omega + \frac{V_{\mathrm{ref}}}{D_c}\right)^{-1}\left(V_{p1}\frac{\partial\theta_0}{\partial x} + V_{p0}\frac{\partial\theta_1}{\partial x}\right). \quad \text{(B11)}$$

The term multiplied by V_1/V_{ref} accounts for the friction law and the local change in state, and the second term accounts for the friction law and the advection of the state profile. When we examine the magnitude of each of the terms on the right-hand side in the simulations, the term that is multiplied by V_1/V_{ref} is the largest. We obtain a good approximation for the relation between the periodic components of stress and velocity when we keep only that term, as in equation (10).

Appendix C: Modulation of a Zero-Stiffness Spring Block Slider

[97] We use an approach similar to that in Appendix B to determine the modulation of the zero-stiffness spring block slider introduced in section 4.1. We use the first-order equations for the friction law (equation (B6)) and for the state evolution law (equation (B7)). In this case, we do not have to consider propagation. The reference $V_{\mathrm{ref}}\theta_0/D_c = 1$, so the state evolution law (equation (B7)) becomes

$$i\omega\theta_1 \approx -\frac{V_{\mathrm{ref}}\theta_1}{D_c} - \frac{V_1\theta_0}{D_c}. \quad \text{(C1)}$$

Inserting this into the friction law (equation B6) gives

$$\tau_1 \approx \frac{V_1}{V_{\mathrm{ref}}}\left(a\sigma - b\sigma\frac{V_c}{V_c\theta_0 + D_c}\left(i\omega + \frac{V_{\mathrm{ref}}}{D_c}\right)^{-1}\right). \quad \text{(C2)}$$

Appendix D: Elastic Interactions Due to Tidally Modulated Slip

D1. Along-Strike Variations in Modulation

[98] Typically, the fractional modulation is a factor of a few larger well behind the front than it is closer to the front, as seen in Figure 6c. This means that by the time of the peak slip rate, slip rates farther behind the front have increased by a larger factor than slip rates nearer the front. These changes in slip rate cause a positive stressing rate near the front and a negative stressing rate farther behind the front at this time. The accumulated stress lags the stressing rate by 90°, so if we add this stressing rate to the applied tidal load, the peak stress occurs later near the front and earlier farther behind the front. The advances and delays of peak stress are present

in the simulation in Figure 6, as seen in the blue x's within $0.2W$ of the front in Figure 6d.

[99] Because of the changes in the timing of the peak stress, the peak velocity also occurs earlier farther behind the front (red x's within $0.15W$ of the front in Figure 6d). As noted in section 4.3.1, the open squares in Figures 6c and 6d are predictions of the velocity modulation that account for both the applied tidal forcing and the elastic interactions due to tidal slip. Those predictions are slightly better than the predictions that account only for the applied tidal forcing (open circles). To make them, we simply extract the periodic component of stress from the simulations. We do not attempt to quantify the elastic interactions without running the simulations.

[100] In the simulation in Figure 6, the elastic stresses due to tidally modulated slip are much smaller than the tidal forcing, and their effect on the modulation of velocity is minor. In simulations with longer tidal periods and smaller W, the elastic stresses due to tidally modulated slip can approach the magnitude of the tidal forcing, and these stresses have a major effect on the modulation of the slip rate. We examine this effect in sections D2 and D3. As we change the parameters to favor larger elastic interactions, the fractional modulation of the slip rate becomes more uniform. Regardless of the simulation parameters we supply, the magnitude of the elastic interactions due to tidally modulated slip does not exceed the magnitude of the applied load.

D2. Plausible Magnitude

[101] Tidally modulated slip creates additional elastic tidal stresses when the fractional magnitude of slip rate in the region near steady state changes with distance behind the front. To obtain a rough estimate of this stress change, we approximate that the region near steady state is composed of two sections. The first section spans the region within L_m of the front. It has uniform slip rate V_{near} and fractional modulation $\Delta V_{\text{near}}/V_{\text{near}}$. The second section has uniform slip rate V_{far} and fractional modulation $\Delta V_{\text{far}}/V_{\text{far}}$. This second section should terminate at the trailing edge of the region near steady state, but we seek only an order of magnitude estimate of the stress change due to spatially variable modulation, so for simplicity we assume that it extends from L_m to infinity behind the front. We also assume that the fractional modulation of the propagation velocity, $\Delta V_{\text{prop}}/V_{\text{prop}}$, is equal to $\Delta V_{\text{near}}/V_{\text{near}}$, since in simulations the modulation of V_{prop} is usually close to the modulation not far behind the front (Appendix E).

[102] As noted in Appendix E, a uniform fractional change in slip rate and propagation velocity does not change the shape of the propagating stress profile. The stressing rate that does cause a change in the stress profile comes from the modulation of the slip rate in the second section, which differs from $\Delta V_{\text{prop}}/V_{\text{prop}}$. If the slip and propagation rates vary sinusoidally, the stressing rate at the center of the section closer to the front is

$$\dot{\tau} = \mu \left(\frac{\Delta V_{\text{far}}}{V_{\text{far}}} - \frac{\Delta V_{\text{near}}}{V_{\text{near}}} \right) \frac{V_{\text{far}} \pi}{L_m} \sin\left(\frac{2\pi t}{T_t} \right), \qquad \text{(D1)}$$

where $t = 0$ is the phase of the maximum slip rate. In this calculation, we have assumed a 2-D anti-plane strain geometry rather than accounting for the strip model. The difference is unimportant for rough estimates of elastic interactions on length scales smaller than W. If we assume that the front does not propagate significantly during the tidal period, the accumulated stress in the center of the section closer to the front is

$$\Delta\tau = \mu \left(\frac{\Delta V_{\text{far}}}{V_{\text{far}}} - \frac{\Delta V_{\text{near}}}{V_{\text{near}}} \right) \frac{V_{\text{far}} T_t}{2L_m} \cos\left(\frac{2\pi t}{T_t} \right). \qquad \text{(D2)}$$

In fact, the front does propagate. To correctly calculate the accumulated stress, we should account for both the stressing rate given by equation (D1) and for advection. The stress accumulated from tidally modulated slip varies spatially, so the stress accumulation predicted by equation (D2) is usually an overestimate.

[103] Equation (D2) nevertheless illustrates the parameters that control the magnitude of the elastic interactions. Elastic interactions are large when there are large spatial variations in fractional modulation and when the ratio of the slip per tidal cycle to the length scale for changes in modulation (L_m) is large. The stress change is therefore large when the slip rate is high, the tidal period is long, and L_m is small.

[104] L_m must be smaller than the region near steady state, which is typically 0.2 to $0.5W$ in cycle simulations. In Cascadia, W is 50 to 100 km [e.g., *Wech et al*., 2009; *Obara*, 2010; *Schmidt and Gao*, 2010], so a plausible length scale for variations in fractional modulation L_m is around 10 km. If we assume that the larger modulation $\Delta V_{\text{far}}/V_{\text{far}}$ is 30% and that the smaller modulation $\Delta V_{\text{near}}/V_{\text{near}}$ is 15%, and then take a slip rate V_{far} of 10^{-7} m/s, a shear modulus μ of 30 GPa, and a tidal period T_t of 12 hours, the elastic interactions are, at most, of order 1 kPa. The direct tidal forcing in this region is also around 1 kPa [e.g., *Lambert et al*., 2009; *Hawthorne and Rubin*, 2010], so the elastic stresses due to tidally modulated slip may or may not be important for Cascadia.

D3. Limited Magnitude of Elastic Interactions

[105] Equation (D2) predicts that if W were sufficiently small and the tidal period were sufficiently long, the elastic interactions due to tidally modulated slip could be much larger than the applied load. However, we find that no matter which model parameters we use, the summed tidal stresses never greatly exceed the applied load. In fact, we can see relatively quickly that the friction law and elasticity do not allow for a solution when elastic interactions dominate the tidally varying stress. According to elasticity, the most negative stressing rate in the region with larger modulation should occur at the time of its maximum slip rate. This implies that the maximum slip rate should be 90° after the maximum stress. According to the friction law, the maximum stress and maximum slip rate should be at nearly the same time. For example, when the slip rate is larger than $2V_{\tau\text{-min}}$, the slip rate should peak at most 60° after the maximum stress (Figure 8). To avoid this inconsistency, we must account for the applied tidal load.

[106] In simulations with parameters that favor large elastic interactions, the fractional modulation in the region near steady state becomes relatively uniform. One example of this behavior can be seen in the simulation shown in Figure D1, where the red x's, which indicate the modulation of the slip rate, plot close to a horizontal line in Figures D1c

and D1d. The magnitude of the modulation in the region near steady state is around $4A_t/a\sigma$. That magnitude is close to the predicted response to the direct tidal forcing (open circles) at slip rates around $3V_{\tau\text{-min}}$, which are present $0.1W$ behind the front, but it is quite a bit larger than the predicted response at higher slip rates. The friction law does a better job of predicting the modulation at all velocities when we predict the modulation using the stresses extracted from the simulations, which include the stresses associated with elastic interactions (open squares). In this context, the fractional modulation of slip rate is roughly uniform because the magnitude of the tidally varying stress decreases with distance behind the front.

[107] That decrease arises because the modulation is not quite uniform. We determine the slip rate modulation that contributes to these elastic stresses by subtracting the cosine and sine components of the modulation of velocity in each bin from the modulation of the propagation velocity (horizontal tan dashed lines). The remaining slip rate modulation is indicated by the green x's in Figures D1c and D1d. The peak slip rate in this component of the modulation occurs about 90° before the maximum applied tidal stress, but it is larger farther behind the front. At the time of its peak, this slip rate modulation contributes a negative stressing rate farther from the front and a positive stressing rate closer to the front. Those stressing rates enhance the applied load close to the front and diminish it farther from the front. When coupled with the friction law, those stresses allow for the nearly uniform modulation of the slip rate.

[108] They do not, however, explain the 45° delay in the maximum stress and slip rate throughout the region near steady state. That delay arises at least in part because the back-propagating fronts impart some stress on the region near steady state. Understanding the stress contributions from the back-propagating fronts is beyond the scope of this study.

D4. Stress Drop Driving Back-Propagating Fronts From Spatially Variable Modulation

[109] In simulations where the tidal period is longer than about $10D_c/V_{\tau\text{-min}}$, the quasi-sinusoidal modulation of slip rate in the region below steady state is typically smaller than the modulation near steady state (sections 4.3.1 and 4.3.2). Slip rates reach a maximum around the time of the maximum applied tidal stress in both regions, but the slip rate in the region near steady state increases more. This creates a positive stressing rate in the region below steady state during this part of the tidal cycle. The positive stressing rate favors the nucleation and continued propagation of back-propagating fronts. However, the stress accumulated from the sinusoidally varying stressing rate is near zero at the time of the maximum applied stress, when the back-propagating fronts are usually strongest. The accumulated stress reaches its maximum one-quarter cycle later. Back-propagating fronts often stall well before that time, so much of the stress associated with spatially variable modulation is unavailable to them.

[110] We can nevertheless obtain an upper bound on the elastic stress associated with the spatially variable modulation. Following the approach in section D2, we approximate that the entire region near steady state has a single fractional modulation equal to the modulation of the propagation velocity. We assume that the region below steady state experiences no modulation. This will allow us to estimate the maximum possible stress accumulation that might drive the back-propagating fronts. With these assumptions, the stress a distance L_{behind} behind the region near steady state achieves a maximum increase of less than $\mu V_{\tau\text{-min}} T_t/4L_{\text{behind}}$ times the half-amplitude of the fractional modulation in the region near steady state. Here $V_{\tau\text{-min}}$ is an upper bound on the slip rate in the region below steady state. In Cascadia, the mean slip rate is around 10^{-7} m/s, [e.g., *Wech et al*., 2009; *Bartlow et al*., 2011; *Dragert and Wang*, 2011], which would imply that $V_{\tau\text{-min}}$ is a few times 10^{-8} m/s. The strongest tidal response is at a period T_t of about 12 h $\approx 4 \times 10^4$ s [*Hawthorne and Rubin*, 2010; *Klaus*, 2011]. If we take a shear modulus μ of 30 GPa, a modulation of 25% [*Hawthorne and Rubin*, 2010], and assume that L_{behind} is half the size of the shortest back-propagating front, or 15 km [*Obara*, 2010; *Houston et al*., 2011; *Obara et al*., 2012], an upper bound on the stress change is 0.1 kPa. The direct tidal shear stress in this region is around 1 kPa [e.g., *Lambert et al*., 2009; *Hawthorne and Rubin*, 2010], so it seems unlikely that the stress change associated with spatially variable modulation makes an important contribution to the stress drop driving back-propagating fronts.

[111] Another upper bound on this contribution, in Cascadia and in the models, comes from the fact that it cannot drive a fractional modulation that is larger than the modulation in the region near steady state. In the event in Figure 6c, and in most other simulations, the modulation in the distance range that exhibits back-propagating fronts is larger than that in the region near steady state. The mechanism here cannot drive much of that modulation, so at least some of the stress drop that drives the back-propagating fronts must come from direct tidal forcing or from the stress recovery.

Appendix E: Modulation of the Propagation Rate

[112] As noted in section 4.3.4, in our simulations the propagation rate varies quasi-sinusoidally, with fractional amplitude and phase similar to those of the modulation of the slip rate not far behind the front, in the region near steady state. That modulation seems reasonable in the context of elasticity. To understand it, note that the stressing rate in a deformable fault model is a linear function of the slip rate. If we consider a scenario where the slip rate everywhere increases by some factor due to tidal forcing, the elastic stressing rate everywhere increases by that factor. This increased stressing rate can be accounted for simply by changing the propagation velocity; it is not necessary to change the slope of the moving stress profile. During propagation of an unchanging stress profile, the stressing rate at any given point equals the slope of the reference stress profile times the propagation velocity. If the propagation velocity increases by the same factor the slip rate increased by, the stressing rate from the more quickly propagating profile will match the expectations from elasticity.

[113] However, this simple solution is for uniform fractional changes in velocity. Modulation is typically larger farther behind the front, as seen in Figure 6. We find that

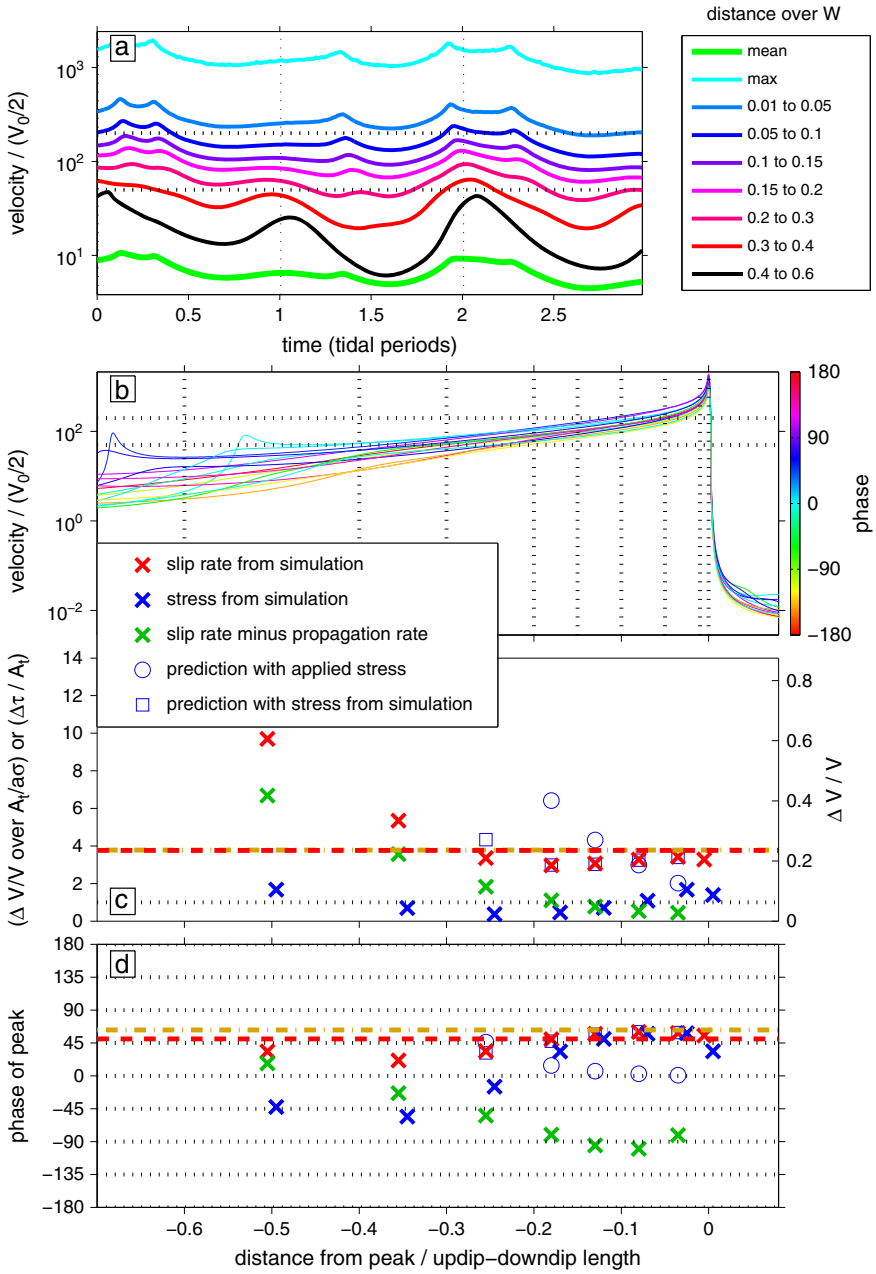

Figure D1. As in Figure 6, but for a simulation where the elastic stresses due to tidal slip are larger. The small peaks in velocity in (a) exist because the main front collides with a set of closely spaced peaks left by back-propagating fronts in the previous slow slip event. These are seen in many tidal simulations, but they do not seem to influence the pattern of slip and stress modulation plotted in (c) and (d), which is consistently observed in simulations where elastic interactions due to tidally modulated slip are important. As seen in (a), (c), and (d), the fractional modulation of slip rate is roughly uniform in the region near steady state (red x's). The green x's indicate the component of the modulation in each bin that deviates from the modulation of the maximum velocity. This component of the slip rate creates elastic stresses that enhance the applied tidal load close to the front and diminish it farther behind the front. This aging law simulation has $a/b = 0.8$, $W/L_b = 250$, no low-normal-stress region, $A_t/b\sigma = 0.05$, and $V_{\tau\text{-min}}T_t/D_c = 75$.

the fractional modulation of the propagation velocity closely matches the smaller modulation near the front.

[114] In the simulations, the modulation of the maximum velocity, V_{max}, is similar to that of the propagation velocity. This is consistent with the $V_{prop} - V_{max}$ relation from equation (7), $V_{prop} = \alpha V_{max}\mu/\Delta\tau_{p\text{-}r}$, which holds throughout the tidal cycle. Typically, V_{max} is larger than $15V_{\tau\text{-min}}$. When V_{max} is this large, the peak to residual stress drop $\Delta\tau_{p\text{-}r}$ varies almost not at all with V_{max} (equation 6). Hence $\Delta\tau_{p\text{-}r}$ varies little as a result of tidal forcing, and the fractional changes in propagation rate are similar to the fractional changes in maximum velocity.

[115] **Acknowledgments.** We thank two anonymous reviewers and the associate editor for comments on the manuscript. This research was supported by NSF grant EAR-0911378. J.C.H. was also supported by a Charlotte Elizabeth Procter Fellowship from Princeton University.

References

Ader, T. J., J.-P. Ampuero, and J.-P. Avouac (2012), The role of velocity-neutral creep on the modulation of tectonic tremor activity by periodic loading, *Geophys. Res. Lett.*, *39*(16), L16310, ISSN 0094-8276, doi: 10.1029/2012GL052326.

Ampuero, J.-P., and A. M. Rubin (2008), Earthquake nucleation on rate and state faults—Aging and slip laws, *J. Geophys. Res.*, *113*, B01302, ISSN 0148-0227, doi:10.1029/2007JB005082.

Bartlow, N. M., S. Miyazaki, A. M. Bradley, and P. Segall (2011), Space-time correlation of slip and tremor during the 2009 Cascadia slow slip event, *Geophys. Res. Lett.*, *38*, L18309, ISSN 0094-8276, doi: 10.1029/2011GL048714.

Bayart, E., A. M. Rubin, and C. Marone (2006), Evolution of fault friction following large velocity jumps, *AGU Fall Meeting Abstracts*, S31A–180, San Francisco, Calif.

Beeler, N. (2009), Constructing constitutive relationships for seismic and aseismic fault slip, *Pure and Appl. Geophys.*, *166*(10), 1775–1798, doi: 10.1007/s00024-009-0523-0.

Bizzarri, A., and M. Cocco (2003), Slip-weakening behavior during the propagation of dynamic ruptures obeying rate- and state-dependent friction laws, *J. Geophys. Res.*, *108*, 2373, doi:10.1029/2002JB002198.

Boettcher, M. S., G. Hirth, and B. Evans (2007), Olivine friction at the base of oceanic seismogenic zones, *J. Geophys. Res.*, *112*, B01205, doi: 10.1029/2006JB004301.

Boyarko, D. C., and M. R. Brudzinski (2010), Spatial and temporal patterns of nonvolcanic tremor along the southern Cascadia subduction zone, *J. Geophys. Res.*, *115*, B00A22, doi:10.1029/2008JB006064.

Brechet, Y., and Y. Estrin (1994), The effect of strain-rate sensitivity on dynamic friction of metals, *Scripta Metallurgica Et Materialia*, *30*(11), 1449–1454.

Creager, K. C., A. J. Klaus, A. Wech, H. Houston, and J. E. Vidale (2011), Nucleation of northern Cascadia episodic tremor and slip events, *AGU Fall Meeting Abstracts*, S33C–01, San Francisco, California.

Dieterich, J. H. (2007), Applications of rate- and state-dependent friction to models of fault slip and earthquake occurrence, in *Treatise on Geophysics, volume 4: Earthquake Seismology*, edited by Kanamori, H., and G. Schubert, Elsevier, Amsterdam, 6054. ISBN 0-444-51928-9.

Dieterich, J. H. (1992), Earthquake nucleation on faults with rate-dependent and state-dependent strength, *Tectonophysics*, *211*(1–4), 115–134, doi: 10.1016/0040-1951(92)90055-B.

Dieterich, J. H. (1978), Time-dependent friction and mechanics of stick-slip, *Pure and Appl. Geophys.*, *116*(4–5), 790–806.

Dieterich, J. H. (1972), Time-dependent friction in rocks, *J. Geophys. Res.*, *77*(20), 3690–3697, doi:10.1029/JB077i020p03690.

Dragert, H., K. L. Wang, and T. S. James (2001), A silent slip event on the deeper Cascadia subduction interface, *Science*, *292*(5521), 1525–1528, doi:10.1126/science.1060152.

Dragert, H., and K. Wang (2011), Temporal evolution of an episodic tremor and slip event along the northern Cascadia margin, *J. Geophys. Res.*, *116*, B12406, doi:10.1029/2011JB008609.

Estrin, Y., and Y. Brechet (1996), On a model of frictional sliding, *Pure and Appl. Geophys.*, *147*(4), 745–762, doi:10.1007/BF01089700.

Ghosh, A., J. E. Vidale, J. R. Sweet, K. C. Creager, and A. G. Wech (2009), Tremor patches in Cascadia revealed by seismic array analysis, *Geophys. Res. Lett.*, *36*, L17316, doi:10.1029/2009GL039080.

Ghosh, A., J. E. Vidale, J. R. Sweet, K. C. Creager, A. G. Wech, and H. Houston (2010a), Tremor bands sweep Cascadia, *Geophys. Res. Lett.*, *37*, L08301, doi:10.1029/2009GL042301.

Ghosh, A., J. E. Vidale, J. R. Sweet, K. C. Creager, A. G. Wech, H. Houston, and E. E. Brodsky (2010b), Rapid, continuous streaking of tremor in Cascadia, *Geochem., Geophys., Geosyst.*, *11*, Q12010, doi: 10.1029/2010GC003305.

Hawthorne, J. C., and A. M. Rubin (2010), Tidal modulation of slow slip in Cascadia, *J. Geophys. Res.*, *115*, B09406, doi: 10.1029/2010JB007502.

Hawthorne, J. C. (2012), *Observations and modeling of temporal variability in slow slip events*, Ph.D., Princeton University, New Jersey.

He, C., W. Yao, Z. Wang, and Y. Zhou (2006), Strength and stability of frictional sliding of gabbro gouge at elevated temperatures, *Tectonophysics*, *427*(1–4), 217–229, doi:10.1016/j.tecto.2006.05.023.

He, C., Z. Wang, and W. Yao (2007), Frictional sliding of gabbro gouge under hydrothermal conditions, *Tectonophysics*, *445*(3–4), 353–362, doi: 10.1016/j.tecto.2007.09.008.

Heslot, F., T. Baumberger, B. Perrin, B. Caroli, and C. Caroli (1994), Creep, stick-slip and dry-friction dynamics: Experiments and a heuristic model, *Physical Review E*, *49*(6), 4973–4988, doi:10.1103/PhysRevE.49.4973.

Houston, H., B. G. Delbridge, A. G. Wech, and K. C. Creager (2011), Rapid tremor reversals in Cascadia generated by a weakened plate interface, *Nat. Geosci.*, *4*(6), 404–409, doi:10.1038/ngeo1157.

Ida, Y. (1973), The maximum acceleration of seismic ground motion, *Bulletin of the Seismological Society of America*, *63*(3), 959–968.

Ide, S. (2010), Striations, duration, migration and tidal response in deep tremor, *Nature*, *466*(7304), 356–359, doi:10.1038/nature09251.

Ide, S. (2012), Variety and spatial heterogeneity of tectonic tremor worldwide, *J. Geophys. Res.*, *117* (B3), B03302, doi: 10.1029/2011JB008840.

Kao, H., S.-J. Shan, H. Dragert, G. Rogers, J. F. Cassidy, K. Wang, T. S. James, K. Ramachandran, and Spatial-temporal patterns of seismic tremors in northern Cascadia (2006), *J. Geophys. Res.*, *111*, B03309.

Kilgore, B. D., M. L. Blanpied, and J. H. Dieterich (1993), Velocity dependent friction of granite over a wide range of conditions, *Geophys. Res. Lett.*, *20*(10), 903–906.

Klaus, A. J., K. C. Creager, J. R. Sweet, and A. G. Wech (2011), Space-time variations in tidal stress and Cascadia tremor amplitude, *AGU Fall Meeting Abstracts*, S23B–2246.

Lambert, A., H. Kao, G. Rogers, and N. Courtier (2009), Correlation of tremor activity with tidal stress in the northern Cascadia subduction zone, *J. Geophys. Res.*, *114*, B00A08, doi:10.1029/2008JB006038.

Lawn, B. (1993), *Fracture of Brittle Solids* 2edition, Cambridge University Press , Cambride, U. K.

Liu, Y. J., and J. R. Rice (2005), Aseismic slip transients emerge spontaneously in three-dimensional rate and state modeling of subduction earthquake sequences, *J. Geophys. Res*, *110*, B08307, doi: 10.1029/2004JB003424.

Liu, Y. J., and J. R. Rice (2007), Spontaneous and triggered aseismic deformation transients in a subduction fault model, *J. Geophys. Res.*, *112*(B9), B09404, doi:10.1029/2007JB004930.

Liu, Y., and J. R. Rice (2009), Slow slip predictions based on granite and gabbro friction data compared to GPS measurements in northern, Cascadia, *J. Geophys. Res.*, *114*, B09407, doi: 10.1029/2008JB006142.

Liu, Y., and A. M. Rubin (2010), Role of fault gouge dilatancy on aseismic deformation transients, *J. Geophys. Res.*, *115*, B10414, doi: 10.1029/2010JB007522.

Luo, Y., and J. P. Ampuero (2011), Numerical simulation of tremor migration triggered by slow slip and rapid tremor reversals, *AGU Fall Meeting Abstracts*, S33C–02, San Francisco, California.

Marone, C. (1998), Laboratory-derived friction laws and their application to seismic faulting, *Annual Review of Earth and Planetary Sciences*, *26*, 643–696, doi:10.1146/annurev.earth.26.1.643.

Matsuzawa, T., H. Hirose, B. Shibazaki, and K. Obara (2010), Modeling short- and long-term slow slip events in the seismic cycles of large subduction earthquakes, *J. Geophys. Res.*, *115*, B12301, doi: 10.1029/2010JB007566.

Moore, D. E., D. A. Lockner, S. Ma, R. Summers, and J. D. Byerlee (1997), Strengths of serpentinite gouges at elevated temperatures, *J. Geophys. Res.*, *102*, 14787–14802.

Moore, D. E., D. A. Lockner, H. Tanaka, K. Iwata, and W. G. Ernst (2004), The coefficient of friction of chrysotile gouge at seismogenic depths, in *Serpentine and Serpentinites: Mineralogy, Petrology, Geochemistry, Ecology, Geophysics, and Tectonics,* volume 8 of *A Tribute to Robert, G. Coleman International Book Series*, 525–538, Bellwether, for Geological Society of America, Columbia, MD.

Nakata, R., N. Suda, and H. Tsuruoka (2008), Non-volcanic tremor resulting from the combined effect of Earth tides and slow slip events, *Nat. Geosci.*, *1*, 676–678, doi:10.1038/ngeo288.

Nakatani, M., and C. H. Scholz (2004), Frictional healing of quartz gouge under hydrothermal conditions: 1. Experimental evidence for solution transfer healing mechanism, *J. Geophys. Res.*, *109*(B7), 19.

Nakatani, M., and C. H. Scholz (2006), Intrinsic and apparent short-time limits for fault healing: Theory, observations, and implications for velocity-dependent friction, *J. Geophys. Res.*, *111*(B12).

Obara, K. (2002), Nonvolcanic deep tremor associated with subduction in southwest Japan, *Science*, *296* (5573), 1679–1681, doi: 10.1126/science.1070378.

Obara, K. (2010), Phenomenology of deep slow earthquake family in southwest Japan: Spatiotemporal characteristics and segmentation, *J. Geophys. Res.*, *115*, B00A25, doi:10.1029/2008JB006048.

Obara, K., T. Matsuzawa, S. Tanaka, and T. Maeda (2012), Depth-dependent mode of tremor migration beneath Kii Peninsula, Nankai subduction zone, *Geophys. Res. Lett.*, *39* (10), L10308, doi: 10.1029/2012GL051420.

Peng, Z., and J. Gomberg (2010), An integrated perspective of the continuum between earthquakes and slow-slip phenomena, *Nat. Geosci.*, *3*(9), 599–607, doi:10.1038/ngeo940.

Perfettini, H., and J. Schmittbuhl (2001), Periodic loading on a creeping fault: Implications for tides, *Geophys. Res. Lett.*, *28*(3), 435–438.

Perfettini, H., J. Schmittbuhl, J. R. Rice, and M. Cocco (2001), Frictional response induced by time-dependent fluctuations of the normal loading, *J. Geophys. Res.-Solid Earth*, *106*(B7), 13455–13472.

Reinen, L. A., J. D. Weeks, and T. E. Tullis (1994), The frictional behavior of lizardite and antigorite serpentinites: Experiments, constitutive models, and implications for natural faults, *Pure and Appl. Geophys.*, *143* (1–3), 317–358, doi:10.1007/BF00874334.

Rubin, A. M., and J. P. Ampuero (2005), Earthquake nucleation on (aging) rate and state faults, *J. Geophys. Res.*, *110*, B11312, doi:10.1029/2005JB003686.

Rubin, A. M. (2011), Designer friction laws for bimodal slow slip propagation speeds, *Geochem., Geophys., Geosyst*, *12*, Q04007, doi:10.1029/2010GC003386.

Rubin, A. M. (2008), Episodic slow slip events and rate-and-state friction, *J. Geophys. Res.*, *113*, B11414, doi:10.1029/2008JB005642.

Rubinstein, J. L., M. La, Rocca, J. E. Vidale, K. C. Creager, and A. G. Wech (2008), Tidal modulation of nonvolcanic tremor, *Science*, *319*(5860), 186–189, doi:10.1126/science.1150558.

Ruina, A. (1983), Slip instability and state variable friction laws, *J. Geophys. Res.*, *88*(B12), 10359–10370, doi:10.1029/JB088iB12p10359.

Ruina, A. L. (1980), *Friction laws and instabilities: a quasistatic analysis of some dry frictional behaviors*, Ph.D., Brown University, Providence RI.

Saffer, D. M., and C. Marone (2003), Comparison of smectite- and illite-rich gouge frictional properties: Application to the updip limit of the seismogenic zone along subduction megathrusts, *Earth and Planetary Science Letters*, *215*(12), 219–235, doi: 10.1016/S0012-821X(03)00424-2.

Schmidt, D. A., and H. Gao (2010), Source parameters and time-dependent slip distributions of slow slip events on the Cascadia subduction zone from 1998 to 2008, *J. Geophys. Res.*, *115*, B00A18, doi:10.1029/2008JB006045.

Schwartz, S. Y., and J. M. Rokosky (2007), Slow slip events and seismic tremor at circum-pacific subduction zones, *Rev. Geophys.*, *45*, RG3004, doi:10.1029/2006RG000208.

Segall, P., and J. R. Rice (1995), Dilatancy, compaction, and slip instability of a fluid-infiltrated fault, *J. Geophys. Res.*, *100*(B11), 22155–22171, doi:10.1029/95JB02403.

Segall, P., A. M. Rubin, A. M. Bradley, and J. R. Rice (2010), Dilatant strengthening as a mechanism for slow slip events, *J. Geophys. Res.*, *115*, B12305, doi:10.1029/2010JB007449.

Shelly, D. R., G. C. Beroza, and S. Ide (2007), Complex evolution of transient slip derived from precise tremor locations in western Shikoku, Japan, *Geochem., Geophys., Geosyst*, *8*, Q10014, doi:10.1029/2007GC001640.

Shibazaki, B., and Y. Iio (2003), On the physical mechanism of silent slip events along the deeper part of the seismogenic zone, *Geophys. Res. Lett.*, *30*(9), 4, doi:10.1029/2003GL017047.

Shibazaki, B., and T. Shimamoto (2007), Modelling of short-interval silent slip events in deeper subduction interfaces considering the frictional properties at the unstable-stable transition regime, *Geophys. J. Int.*, *171* (1), 191–205, doi:10.1111/j.1365-246X.2007.03434.X.

Shibazaki, B., S. Bu, T. Matsuzawa, and H Hirose (2010), Modeling the activity of short-term slow slip events along deep subduction interfaces beneath Shikoku, southwest Japan, *J. Geophys. Res.*, *115*, B00A19, doi:10.1029/2008JB006057.

Shimamoto, T. (1986), Transition between frictional slip and ductile flow for halite shear zones at room temperature, *Science*, *231*(4739), 711–714, doi:10.1126/science.231.4739.711.

Shimamoto, T., and J. M. Logan (1986), Velocity-dependent behavior of simulated halite shear zones: An analog for silicates, in *Earthquake source mechanics,* volume 6 of *Geophysical Monographs*, edited by Das, S., J. Boatwright, and C. H. Scholz, 49–63, American Geophysical Union, Washington D.C.

Suzuki, T., and T. Yamashita (2009), Dynamic modeling of slow earthquakes based on thermoporoelastic effects and inelastic generation of pores, *J. Geophys. Res.*, *114*, B00A04, doi:10.1029/2008JB006042.

Szeliga, W., T. Melbourne, M. Santillan, and M. Miller (2008), GPS constraints on 34 slow slip events within the, Cascadia subduction zone, 1997–2005, *J. Geophys. Res.*, *113*, 04404, doi:10.1029/2007JB004948.

Thomas, A. M., R. Burgmann, D. R. Shelly, N. M. Beeler, and M. L. Rudolph (2012), Tidal triggering of low frequency earthquakes near Parkfield, California: Implications for fault mechanics within the brittle-ductile transition, *J. Geophys. Res.*, *117*, B05301, doi:10.1029/2011JB009036.

Thomas, A. M., R. M. Nadeau, and R. Burgmann (2009), Tremor-tide correlations and near-lithostatic pore pressure on the deep San Andreas fault, *Nature*, *462* (7276), 1048–1051, doi:10.1038/nature08654.

Wech, A. G., and K. C. Creager (2008), Automated detection and location of Cascadia tremor, *Geophys. Res. Lett.*, *35*, L20302, doi:10.1029/2008GL035458.

Wech, A. G., K. C. Creager, and T. I. Melbourne (2009), Seismic and geodetic constraints on, Cascadia slow slip, *J. Geophys. Res.*, *114*, B10316, doi:10.1029/2008JB006090.

Weeks, J. D. (1993), Constitutive laws for high-velocity frictional sliding and their influence on stress drop during unstable slip, *J. Geophys. Res.*, *98*(B10), 17,637–17,648, doi:10.1029/93JB00356.

Weeks, J. D., and T. E. Tullis (1985), Frictional sliding of dolomite: A variation in constitutive behavior, *J. Geophys. Res.*, *90*(B9), 7821, doi:10.1029/JB090iB09p07821.

Yamashita, T., and T. Suzuki (2011), Dynamic modeling of slow slip coupled with tremor, *J. Geophys. Res.*, *116*, B05301, doi:10.1029/2010JB008136.